Large-Scale State and Evolution of the Atmosphere and Ocean during PISTON 2018

ADAM H. SOBEL,[a,b] JANET SPRINTALL,[c] ERIC D. MALONEY,[d] ZANE K. MARTIN,[d] SHUGUANG WANG,[a] SIMON P. DE SZOEKE,[e] BENJAMIN C. TRABING,[d] AND STEVEN A. RUTLEDGE[d]

[a] *Department of Applied Physics and Applied Mathematics Columbia University, New York, New York*
[b] *Lamont-Doherty Earth Observatory, Columbia University, New York, New York*
[c] *Scripps Institution of Oceanography, La Jolla, California*
[d] *Department of Atmospheric Science, Colorado State University, Fort Collins, Colorado*
[e] *College of Earth, Ocean, and Atmospheric Sciences, Oregon State University, Corvallis, Oregon*

(Manuscript received 9 July 2020, in final form 20 February 2021)

ABSTRACT: The Propagation of Intraseasonal Tropical Oscillations (PISTON) experiment conducted a field campaign in August–October 2018. The R/V *Thomas G. Thompson* made two cruises in the western North Pacific region north of Palau and east of the Philippines. Using select field observations and global observational and reanalysis datasets, this study describes the large-scale state and evolution of the atmosphere and ocean during these cruises. Intraseasonal variability was weak during the field program, except for a period of suppressed convection in October. Tropical cyclone activity, on the other hand, was strong. Variability at the ship location was characterized by periods of low-level easterly atmospheric flow with embedded westward propagating synoptic-scale atmospheric disturbances, punctuated by periods of strong low-level westerly winds that were both connected to the Asian monsoon westerlies and associated with tropical cyclones. In the most dramatic case, westerlies persisted for days during and after tropical cyclone Jebi had passed to the north of the ship. In these periods, the sea surface temperature was reduced by a couple of degrees by both wind mixing and net surface heat fluxes that were strongly ($\sim$200 W m^{-2}) out of the ocean, due to both large latent heat flux and cloud shading associated with widespread deep convection. Underway conductivity–temperature transects showed dramatic cooling and deepening of the ocean mixed layer and erosion of the barrier layer after the passage of Typhoon Mangkhut due to entrainment of cooler water from below. Strong zonal currents observed over at least the upper 400 m were likely related to the generation and propagation of near-inertial currents.

KEYWORDS: Atmosphere-ocean interaction; Hurricanes/typhoons; Monsoons; Tropical variability

1. Introduction

The western North Pacific comprises a large fraction of the so-called warm pool in the Northern Hemisphere. In this region deep convection is active over a very large area, particularly in northern summer and fall. The low-level westerly winds of the Asian monsoon circulation span the region from the Indian Ocean to Southeast Asia into the west Pacific. More tropical cyclones form in the western North Pacific than anywhere else in the world (e.g., Ramsay 2017). On the intraseasonal time scale, the boreal summer intraseasonal oscillation (BSISO) is associated with active and break cycles of the South and East Asian monsoons (e.g., Wang and Xie 1997; Lee et al. 2013). The BSISO has been implicated in the modulation of tropical cyclones across the tropics (e.g., Kikuchi and Wang 2010) and is associated with prominent teleconnections to the extratropics (Moon et al. 2013). The atmosphere and ocean exhibit variability on a broad range of time and space scales in this region, and understanding what processes control these variations is relevant to regional and large-scale climate variability, natural hazards, and local resource management.

The goal of the Propagation of Intraseasonal Tropical Oscillations (PISTON) project was to better understand the mechanisms that modulate atmospheric convection on multiple scales. Key issues that PISTON aimed to address included how heat is stored and released in the upper ocean on intraseasonal time scales, how that heat storage interacts with atmospheric convection, and what role it plays in BSISO maintenance and propagation. Additionally, PISTON aimed to identify processes to which model simulations of the BSISO are particularly sensitive, with the goal of improving their representation in order to advance prediction.

In the late northern summer and early fall of 2018, the first of two field campaigns was carried out in the western North Pacific Ocean for the PISTON project. (A second, more abbreviated PISTON field campaign occurred in the vicinity during the summer of 2019 but is not addressed here.) The R/V *Thomas G. Thompson* was instrumented to make a broad range of observations of the atmosphere, upper ocean, and the interface between them. Because of unexpected logistical challenges, and failing to gain approval for an international Marine Science Research agreement, the original focus region of PISTON was changed from the South China Sea, west of the

Supplemental information related to this paper is available at the Journals Online website: https://doi.org/10.1175/JCLI-D-20-0517.s1.

Corresponding author: Adam Sobel, ahs129@columbia.edu

DOI: 10.1175/JCLI-D-20-0517.1

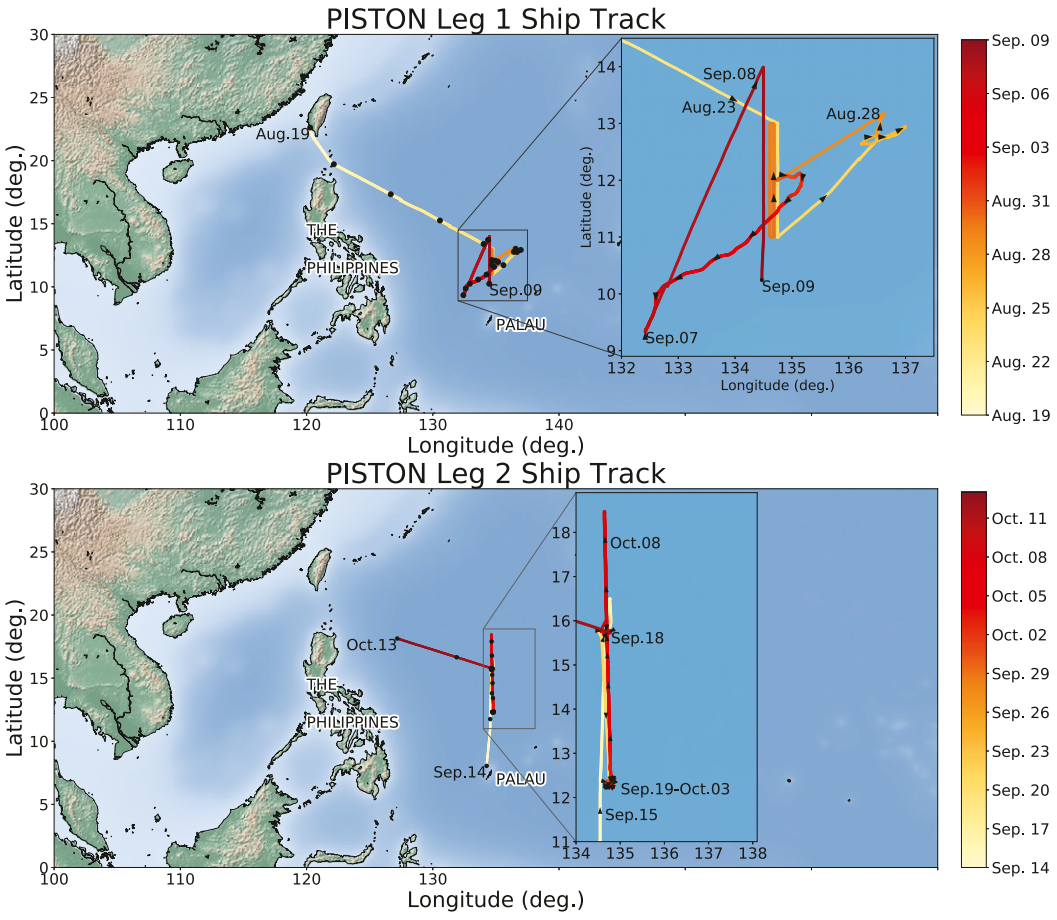

FIG. 1. Ship tracks for the (top) first and (bottom) second legs of the PISTON 2018 field campaign. Note blow up insets to right. Color bar indicates the progression of time, with black dots/arrows indicating the daily location (at 0000 UTC).

Philippines, to the open international waters east of the Philippines. The 2018 field campaign consisted of two legs. In leg 1, the *Thompson* sailed on 19 August from Kaohsiung, Taiwan, to the study region around 10°N, 135°E, north of Palau and east of the Philippines. This region was chosen because it was in international waters, in a region of frequent deep convection and where the BSISO typically has an influence, yet south of typical tropical cyclone tracks. Operations were briefly paused for a resupply and change of personnel in Palau from 10 to 14 September. Leg 2 resumed from Palau and resurveyed the same general area before the ship returned to Kaohsiung, finishing the 2018 field campaign on 15 October. The tracks taken by the *Thompson* in each of these two legs are shown in Fig. 1.

The BSISO was largely inactive during the time of the ship observations (at least by most standard definitions, as described below), so the scientific foci of PISTON investigations have necessarily evolved. In addition, the PISTON field observations covered only a relatively small geographical area, as is typical of field campaigns. As such, we view it as useful to describe the large-scale context in which the observations were taken. The processes occurring in the concentrated field area are of interest, in large part, because they are relevant to the physics of the warm pool's atmosphere–ocean system on larger scales. In this paper, we first present the state and evolution of the atmosphere and upper ocean on scales much larger than those of the PISTON observations. We then describe a subset of the shipboard observations to illustrate possible relationships to the large-scale climate system. Our goal is for the large-scale background presented here to provide context for the interpretation of the field observations, as well as for the complementary modeling studies that integrate the observations, and to help refine the scientific questions and identify opportunities to which the PISTON field observations can best be applied.

2. Atmospheric and oceanic datasets

a. *Gridded analyses*

The fifth generation of ECMWF atmospheric reanalyses of the global climate (ERA5), with a horizontal resolution of 31 km, is used in the study to assess the large-scale atmospheric state during the time period of the field campaign (Hersbach et al. 2020). The temporal resolution used here is daily, with each day represented by the instantaneous field at 0000 UTC. Climatologies were computed daily for the ERA5 period, 1979–2018, and are shown on a 2.5° × 2.5° grid. The NOAA

outgoing longwave radiation (OLR) product was used to diagnose deep convective variability (Liebmann and Smith 1996) and coordinated with satellite imagery from *Himawari-8*. Precipitation data are from the Tropical Rainfall Measuring Mission (TRMM; Liu et al. 2012) version 7 data product: we use the Level 3 daily TRMM-3B42 data from 1 January 1998 to 27 February 2019. The data are retrieved at 0.25° resolution, but are regridded onto the same common 2.5° × 2.5° grid as other fields. Tropical cyclone best tracks are provided by the Joint Typhoon Warning Center (JTWC). Tropical cyclones are classified using the Saffir–Simpson wind speed scale based on one-minute maximum sustained wind estimates (Schott et al. 2019). JTWC designates a tropical cyclone as a super typhoon when maximum wind speeds at the surface reach 67 m s^{-1}.

Sea surface temperature (SST) data are from the daily blended Advanced Very High-Resolution Radiometer product of Optimum Interpolation Sea Surface Temperature version 2 (OISST; Reynolds et al. 2007; Banzon et al. 2016). The horizontal resolution of these gridded data is 0.25° latitude × 0.25° longitude and we used data from 1982 to 2019. The optimally interpolated SST fields are constructed based on an aggregate of buoy, ship, and satellite SST data collected over the entire day. They are representative of the bulk temperature at 1 m. SST anomalies in the Pacific Ocean over the PISTON period were formed by removing the daily mean SST climatology from 1982 to 2019 calculated within each spatial grid box.

b. *In situ measurements during PISTON 2018*

In this study, only a subset of observations taken during PISTON are used. We describe here only that subset.

Global Positioning System (GPS) soundings of tropospheric pressure, temperature, relative humidity, and winds were deployed from the *Thompson* typically every 3 h during the two legs of the 2018 field campaign. Balloons burst at varying altitudes, but usually bore the sensors well above 20 km, in the stratosphere. Sounding data were both objectively and subjectively quality controlled according to the procedures of Ciesielski et al. (2014).

Surface meteorology, including surface air temperature and humidity, SST, surface wind, and precipitation, was measured aboard the *Thompson* by the NOAA Physical Sciences Laboratory surface flux system (Fairall et al. 2012; de Szoeke et al. 2015). Ocean temperature was measured at 5-m depth by the ship's hull-mounted thermosalinograph and at 0.1-m depth by a floating sea snake thermistor. Sensible and latent (evaporative) heat fluxes and wind stress were computed using the COARE 3.5 bulk aerodynamic formula (Edson et al. 2013). Ocean skin temperature is obtained using the COARE algorithm (Fairall et al. 1996). Downwelling solar and thermal infrared radiative fluxes were measured by radiometers on the ship. Upwelling radiative fluxes from the surface were modeled using a constant emissivity (0.97) and the Payne (1972) ocean surface albedo parameterization. Precipitation rate is measured with an Optical Scientific, Inc. optical rain gauge. Most meteorological variables were sampled each second, quality controlled, and then averaged to 10-min means.

Oceanic temperature and salinity profiles were obtained using an underway conductivity–temperature–depth (uCTD) system to provide measurements of the upper ocean stratification. The uCTD permits fast temporal and high spatial resolution while the ship is underway. Profiles were obtained to 400 m every 15 min at a vessel speed of 10 kt (1 kt ≈ 0.51 m s^{-1}), amounting to a profile every 2.5 nautical miles (n mi; 1 n mi = 1.852 km). In all, 267 uCTD profiles were obtained, primarily during five meridional transects completed along roughly 135°E (four transects in leg 1 and one transect in leg 2). All uCTD profiles were quality controlled for salinity spiking and processed according to Ullman and Hebert (2014).

The *Thompson* measured underway upper ocean velocity with 75-kHz narrowband and broadband shipboard acoustic Doppler current profilers (ADCPs) mounted in the hull. Here we use the narrowband currents, sampling from ~28-m depth to 980 m with vertical bins of 16 m. Shipboard ADCP velocity data were processed and calibrated using the CODAS (Common Ocean Data Access System) software.

c. *A note on terminology for winds and currents*

In physical oceanography, the currents are labeled by the direction they are flowing toward: eastward and northward currents move toward the east and north, for example. In atmospheric science, on the other hand, it is customary to label winds by the direction from which they blow, such that a westerly wind is from the west (but toward the east). In this paper, we follow the conventions appropriate to what is being discussed, the atmosphere or the ocean circulation. We use the oceanographic convention for ocean currents, and also for the direction of propagation of features in the atmosphere (e.g., the Madden–Julian oscillation propagates eastward). Because it is standard in the atmospheric literature, we use the atmospheric convention for winds, even though it is the opposite of the oceanographic convention. To reduce confusion, we include the adjective "atmospheric" or the word "wind" wherever "westerly" or "easterly" are used and the meaning is not apparent from context (e.g., as when the terms are used repeatedly in close succession).

3. Results and discussion

a. *Atmospheric conditions*

Figure 2a shows August–October climatologies of 850-hPa wind, 850-hPa geopotential height, and precipitation over the Indian Ocean and western Pacific warm pool. Winds follow the Northern Hemisphere monsoon pattern, with cross-equatorial flow over the western Indian Ocean, and westerly winds over the north Indian Ocean, Indian subcontinent, and Southeast Asia. Over the western North Pacific, the westerly winds slacken and are met at ~160°E by easterlies from the central Pacific. The precipitation has a broad maximum in the Northern Hemisphere from around the Bay of Bengal to 150°E, modulated on smaller scales by coastlines and mountains. A narrow intertropical convergence zone occurs to the east of 150°E nearer to the equator, with additional precipitation maxima over the south Indian Ocean and southern Pacific convergence zone. The PISTON region in particular lies approximately in the western North Pacific precipitation maximum, where climatological mean winds are weak in magnitude and—in the presence of synoptic and subseasonal variability—variable in direction.

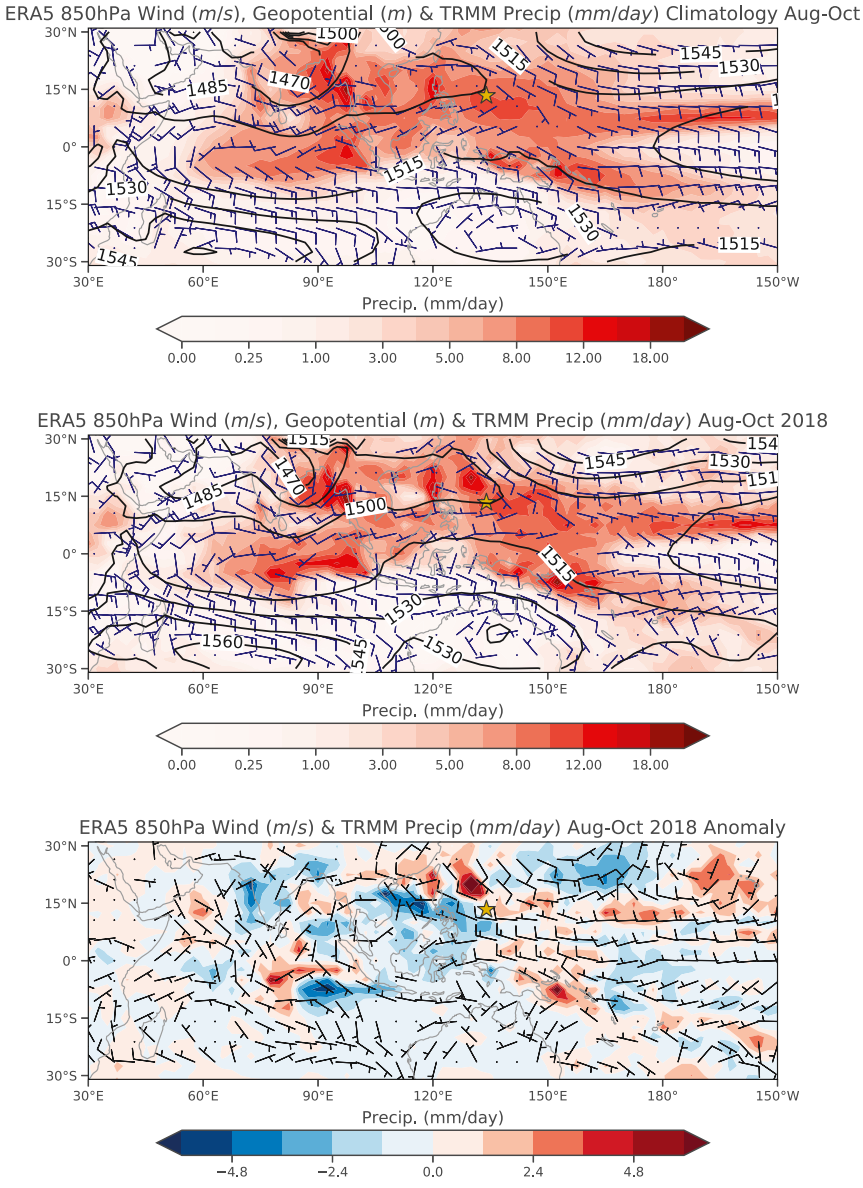

FIG. 2. (top) Climatology, (middle) 2018 values, and (bottom) anomalies computed as the difference between the two, of 850-hPa wind (barbs; m s^{-1}) and precipitation (shading; mm day^{-1}) for August–October. The top two panels also show geopotential height (contours; contour interval 15 m). In the top two panels, a half barb is 2.5 m s^{-1}, and a full barb is 5 m s^{-1}. In the bottom panel, a half barb is 1 m s^{-1} and a full barb is 2 m s^{-1}. The gold star indicates the mean position of the *Thompson*.

Figure 2b shows the August–October 2018 distributions of 850-hPa wind, 850-hPa geopotential height, and precipitation. Figure 2c shows the anomalies of the wind and precipitation fields during this 2018 period relative to the long-term average (Fig. 2a). During 2018, the PISTON region was characterized by anomalous westerly winds to the south of 15°N that extend eastward past 150°E, where they are associated with weakened trade winds and likely consistent with the warm SST anomalies in the central equatorial Pacific (discussed below). Precipitation anomalies were generally weak, although precipitation was slightly enhanced to the east of the PISTON domain and suppressed to the west over the Philippines.

To characterize the variability in these fields further, we present longitude–time Hovmöller plots of total OLR and OLR anomalies averaged from 5° to 20°N during the PISTON period (Fig. 3), with the approximate longitudinal location of the ship when intensive operations occurred denoted by the vertical line along ~135°E. The OLR variability is predominantly on the synoptic to subseasonal time scale, and the propagation of anomalies is mostly westward rather than eastward.

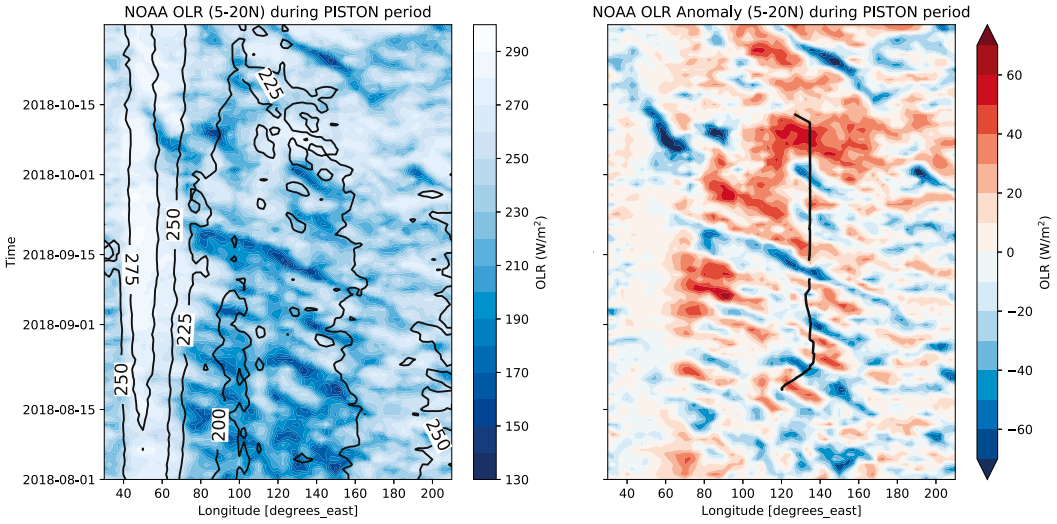

FIG. 3. Longitude–time Hovmöller plots of (left) NOAA OLR (W m^{-2}) and (right) OLR anomaly with respect to daily climatology averaged between 5°–20°N during the PISTON field program. Contours in the left panel indicate the daily climatology. In the right panel, positive (red) indicates drier regions, negative (blue) indicates wetter regions, and the black lines show the longitude of the *Thompson* during the two legs.

Westward-propagating synoptic events are evident, especially in August and September, with several prominent events passing over the ship. Their time scales are reminiscent of tropical depression–type (TD-type) disturbances that have been extensively diagnosed in the literature (e.g., Reed and Recker 1971; Lau and Lau 1990, 1992; Takayabu and Nitta 1993; Sobel and Bretherton 1999). Some of these disturbances are in fact tropical cyclones, as will be discussed below. Very slow eastward propagation of a dry anomaly is evident toward the end of the period, from late September into early October. Hovmöller plots of total column water vapor from ERA5 are shown in Fig. S1 in the online supplemental material, and are quite similar to those of OLR as shown in Fig. 3, indicating the close correspondence between water vapor and convection.

Hovmöller plots are shown of 850-hPa zonal wind (Fig. 4), 200-hPa zonal wind (Fig. 5), and 850-hPa meridional wind (Fig. 6) averaged from 5° to 20°N. The total 850-hPa zonal wind (Fig. 4, top) shows monsoon westerly winds extending as far east as 150°E, modulated by mostly westward-moving disturbances as shown in the anomalies (Fig. 4, right), until the westerly winds collapse quickly in early to mid-September, being replaced by easterlies. In October, an eastward-propagating easterly 850-hPa zonal wind anomaly is evident (Fig. 4). A Hovmöller plot of 5°–20°N averaged MJO-filtered OLR anomalies (e.g., Wheeler

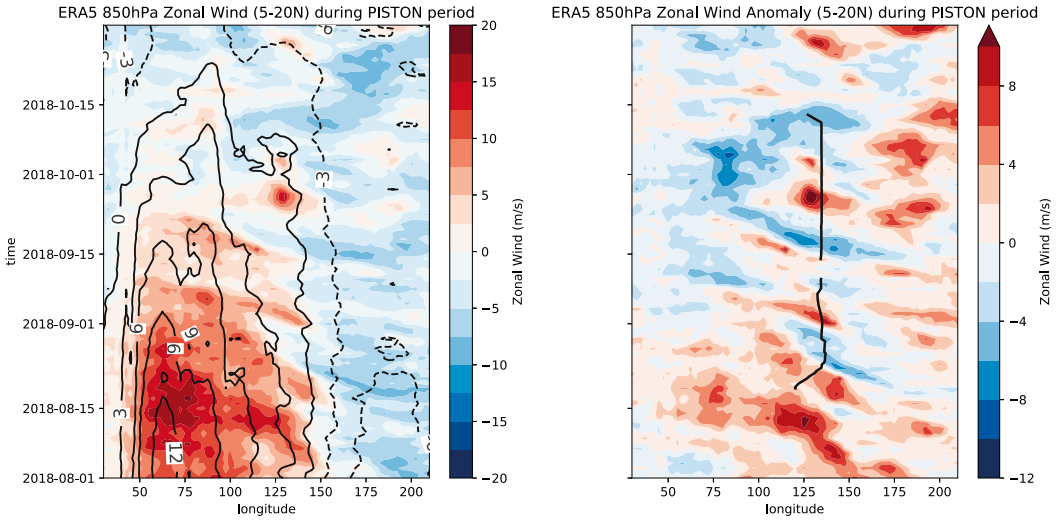

FIG. 4. Longitude–time Hovmöller plots of (left) 850-hPa zonal wind (m s^{-1}) and (right) zonal wind anomaly with respect to daily climatology averaged 5°–20°N during August–October 2018. Contours in the left panel indicate the daily climatology. In the right panel, the black lines indicate the longitude of the *Thompson* during the two legs.

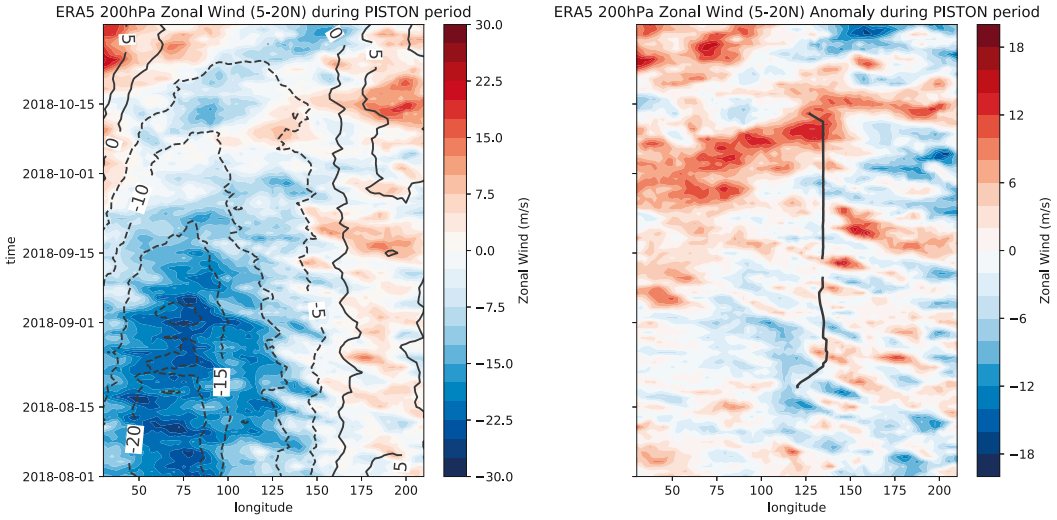

FIG. 5. As in Fig. 4, but for zonal wind (m s^{-1}) at 200 hPa.

et al. 2000), superimposed on the unfiltered OLR anomalies (Fig. 7), indicates that this eastward-propagating signal is associated with a suppressed phase of the MJO. Figure 7 also suggests an active phase before the suppressed phase, in the first half of September, but this is less evident by eye. However, a Hovmöller plot of OLR projected onto the OLR MJO index (OMI; Kiladis et al. 2014) shows that the suppressed phase was much stronger than the active phase (Fig. S2); we suspect that the apparent active phase is largely due to the Gibbs phenomenon, that is, an artifact of the spectral filtering. Figure 7 also shows OLR anomalies filtered to retain the wavenumber–frequency bands corresponding to the equatorial atmospheric Rossby wave (blue) and a combined band for the mixed Rossby–gravity and tropical depression–type (MRG+TD) waves. The spectral bands retained to compute these different wave-filtered anomalies are shown, together with the OLR spectrum, in Fig. S3. Atmospheric Kelvin wave anomalies were also computed, but their amplitudes are too small to be shown with the contour interval of 10 W m^{-2} used for the other waves. The equatorial Rossby and MRG+TD signals will be further discussed below. (For completeness, a plot equivalent to Fig. 7, but averaged 5°S–5°N to be more consistent with the traditional metrics of "equatorial" waves, is shown in Fig. S4; the anomalies are weaker than those in Fig. 7, and are also outside the PISTON domain, so are not discussed further.)

The zonal winds at 200 hPa, both the total winds and the anomalies (Fig. 5), are comparable in magnitude and opposite in direction to those at 850 hPa (Fig. 4) as we might expect for a deep, baroclinic monsoon circulation. The eastward-propagating event in October evident in the OLR anomalies (Figs. 3 and 7) is particularly prominent in the 200-hPa wind anomaly field. On the other hand, examination of the 850-hPa meridional total wind and anomaly

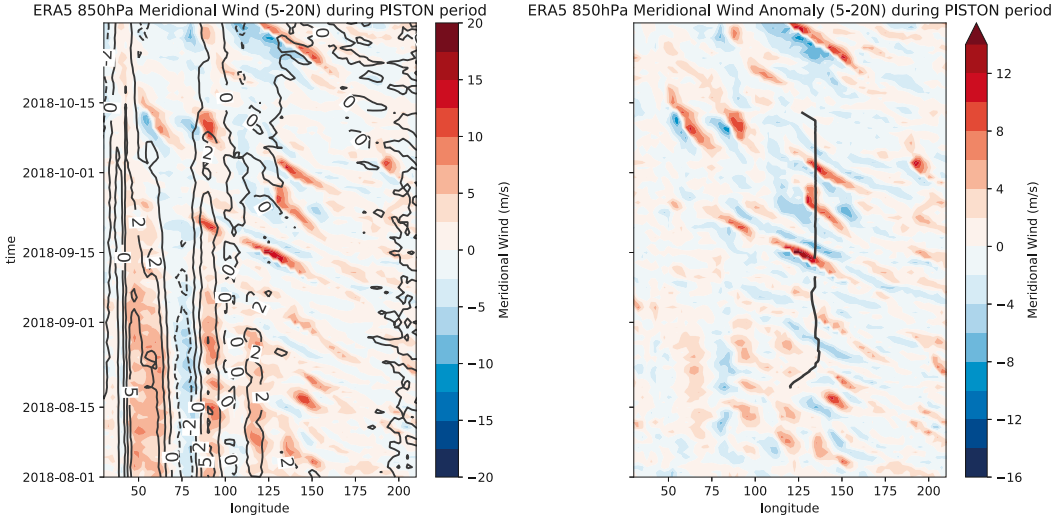

FIG. 6. As in Fig. 4, but for 850-hPa meridional wind (m s^{-1}).

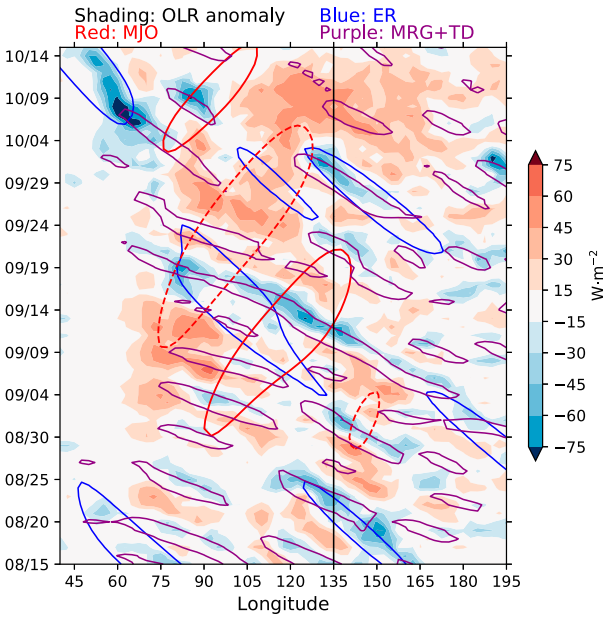

FIG. 7. Hovmöller plot of 5°–20°N OLR ($W\,m^{-2}$), as in Fig. 3, but with superimposed OLR anomalies filtered to preserve the MJO (red; contours −10 and 10 $W\,m^{-2}$), equatorial Rossby wave (blue; contour $-10\,W\,m^{-2}$), and combined mixed Rossby–gravity and tropical depression–type waves (purple; contour $-10\,W\,m^{-2}$). Negative contours are solid; positive are dashed. Filtered Kelvin anomalies are smaller than $-10\,W\,m^{-2}$ and not shown.

(Fig. 6) highlights the strong westward-propagating synoptic variability during the period that was sampled by the ship.

To consolidate the impressions of intraseasonal variability obtained from Figs. 3–7, phase diagrams are presented (Fig. 8) for August–October 2018 from several commonly used indices: the real time multivariate MJO (RMM) index (Wheeler and Hendon 2004), the OMI, the BSISO index of Kikuchi et al. (2012), and the two indices, BSISO1 and BSISO2, from Lee et al. (2013). The months of August, September, and October are indicated by the blue, magenta, and green colors, respectively. Some comparison of these different indices is presented in Wang et al. (2018), with a particular eye to the differences in how each index represents the propagation of the intraseasonal modes. The much smoother trajectories in the OMI and the Kikuchi et al. (2012) index shown in Fig. 8 are partly due to the fact that these are bandpass filtered anomalies projected onto their respective spatial empirical orthogonal function (EOF) modes. The real-time OMI without bandpass filtering is also smoother than RMM or BSISO1/2 (not shown), consistent with the results of Wang et al. (2018). These two smoother indices, preferred by Wang et al. (2018), show weak amplitudes during most of the cruise period. However, the indices emerge from the unit circle in October with a phase such that active convection is occurring in the Western Hemisphere, with suppressed conditions in the Maritime Continent. This behavior is consistent with the positive OLR anomalies in this region during October (Fig. 3).

As noted above, the Hovmöller plot of the OMI-reconstructed OLR averaged over 2.5°–20°N (Fig. S1) confirms the visual impression from Figs. 3–5 that the suppressed phase crossing the PISTON area in late September through early October is intraseasonal, to the extent and in the sense that OMI captures intraseasonal variability. The RMM and BSISO1 indices are noisier, but also consistent in showing the same intraseasonal anomaly at this time; they also indicate larger amplitude in August, in a phase consistent with active convection in the western Pacific, although this is not found in the OMI and Kikuchi et al. (2012) indices. In all, the collection of results from the multiple indices makes clear that assessment of intraseasonal variability is somewhat index-dependent, and that instantaneous amplitude greater than one in a given index is not necessarily indicative of a truly intraseasonal signal—defined, for example, as that which would remain under a 30–90-day bandpass filter—since some indices show considerable high-frequency fluctuations. The excursions outside the unit circle in August in RMM and BSISO1 are examples of such fluctuations.

Figure 9 shows the tracks of all tropical cyclones in the western North Pacific from August to October 2018. The total number of tropical cyclones observed over this period was above the 30-yr August–October average. The period was more extraordinary, however, in that five of the cyclones reached category 5 intensity, a number that has never been exceeded in the previous 30 years, and only reached in one other year, 1997 (Fig. S5), over the same calendar period. In this regard it is relevant that PISTON took place during the onset of an El Niño event (as discussed further below), and that the major El Niño of 1997–98 was also in its onset phase during August–October 1997.

Typhoons Soulik and Cimaron overlapped the experiment primarily during the transit from Taiwan to the PISTON operations area. Typhoon Jebi formed in late August and passed closest to the ship at the beginning of September during leg 1, and then went on to make landfall in Japan, causing great economic and societal damage. Typhoon Mangkhut formed near the end of leg 1, passed near Guam during the Palau port call between legs 1 and 2, and then made a very destructive landfall in the northern Philippines as a category 5 super typhoon. Typhoons Trami and Kong-Rey occurred during leg 2 and both reached super typhoon strength during their life cycles. Typhoon Trami tracked to the north of the observation area around 23 September and intensified to a category 5 super typhoon before stalling out. After the Pacific subtropical ridge intensified, Typhoon Trami regained its steering flow and followed Jebi as the second typhoon to make landfall in Japan within a month. In late September, Typhoon Kong-Rey tracked the closest to the R/V *Thompson* of any tropical cyclone, and quickly intensified to category 5 on the Saffir–Simpson scale. In terms of maximum wind speed, Kong-Rey was tied with Typhoon Yutu, which developed three weeks later, for the strongest tropical cyclone of 2018 in any ocean basin. Super Typhoon Kong-Rey followed a similar track to Trami and appeared to be heavily influenced by the cold water that was upwelled days early, causing Kong-Rey to rapidly weaken (not shown). Kong-Rey later made landfall in South Korea as a tropical storm.

The tropical cyclones that occurred during PISTON 2018, including Jebi, Mangkhut, Trami, and Kong-Rey, are manifest

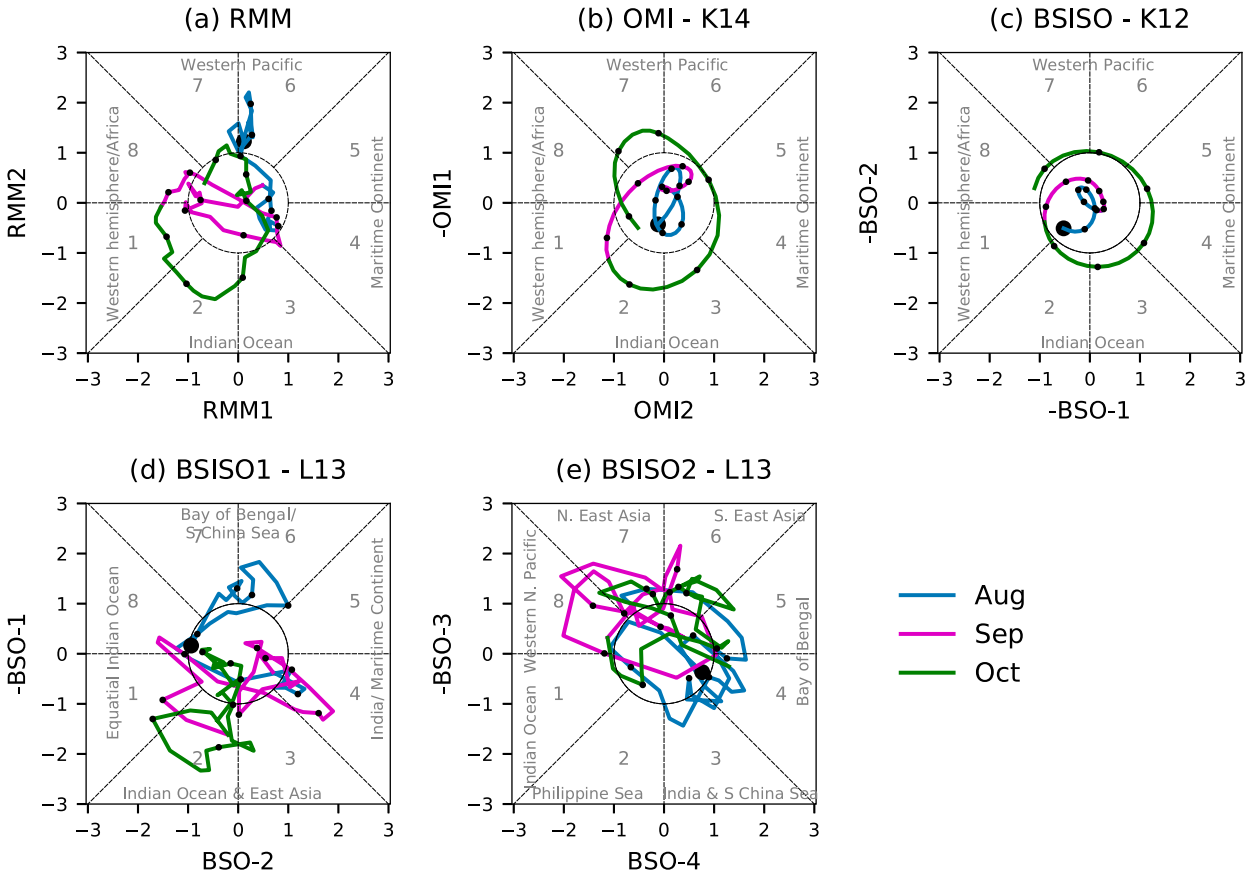

FIG. 8. (a)–(e) Phase diagrams of different indices of the MJO (RMM panel) and BSISO during August–October 2018. For (b)–(e) the title references the first author and year of publication for each index, as described more in the text.

in both the equatorial Rossby and MRG+TD filtered anomalies shown in Fig. 7. (These two bands show very similar phase speeds, but differ in their frequencies, with the MRG+TD occupying the higher frequency band.) Typhoon Mangkhut shows up as a particularly coherent and long-lived signal in both modes. While it is tempting to interpret this by saying that these TCs formed within favorable environments attributable to the large-scale atmospheric wave modes, an equally plausible interpretation may be that the TCs formed for other reasons and, being highly localized in space and time, project widely on any band associated with westward propagation at speeds near their own forward speeds. A causal interpretation of the interaction between TCs and nominally ''larger-scale'' phenomena is at the crux of any dynamical understanding of the large-scale evolution of the atmosphere during PISTON. Such an interpretation is beyond the scope of this descriptive study, however, and likely requires creative numerical modeling in order to untangle cause and effect.

To draw connections between the large-scale structure and evolution in the atmosphere and the local weather experienced at the ship location, Fig. 10 shows time–height plots of fields measured by the soundings launched from the R/V *Thompson*. While the ship did move over much of this period (see Fig. 1), and a small number of soundings from the transit period are included in the figure (the first sounding was launched near 0000 UTC on 21 August, in particular) over nearly all the time shown the ship's displacements were quite small compared to the atmospheric scales of interest here, and these time series can be regarded, for our purposes, as being close to those that would be obtained from a stationary location. Figure 10 shows temperature, zonal and meridional wind, and relative humidity. In each case the time mean of the field at each level (right side of each row in Fig. 10) has been subtracted to produce ''anomalies'' (note that this definition of anomalies is different from the previous figures, which instead used long-term daily climatologies; this is by necessity, since these soundings are available only for the time period shown).

Variability on synoptic time scales—a few days—is evident, as well as longer term, perhaps 10–20-day variability (Fig. 10). Synoptic-scale variability is evident particularly in the meridional wind and relative humidity fields during late August, mid-September (although disrupted by the port call; see Fig. 1), and early October. Given Figs. 3–7, we take these variations to be associated with westward-propagating ''easterly waves'' or in more recent terminology, some combination of TD-type and mixed Rossby–gravity waves, as evident in the MRG+TD band in Fig. 7. The structures in meridional wind during this time show some tendency toward phase reversal with height, as expected for these disturbances (e.g., Reed and Recker 1971; Lau and Lau 1990; Wheeler et al. 2000; Dickinson and Molinari 2002).

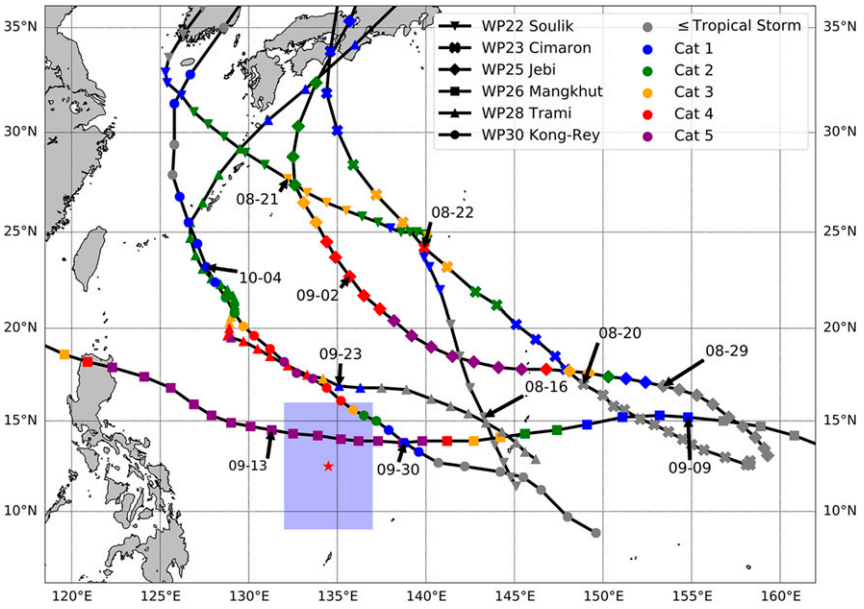

FIG. 9. Tropical cyclone tracks during the PISTON field campaign from JTWC. Each solid mark represents a 6-hourly position along the storm track, and some dates at 0000 UTC are indicated in the figure. The inset legend shows the track identifier of the named storm, with corresponding west Pacific (WP) identification number, and color coding of the Saffir–Simpson wind speed categories. The blue shaded region is the general area of operations during PISTON where observations were collected, and the red star indicates the most common location of the R/V *Thompson* during the cruises, in both cases excluding transit.

The zonal wind shows lower-frequency structure (Fig. 10). Strong westerly wind anomalies are present in the low to mid-troposphere for periods of around 5 days in early September and again in late September, and for a couple of days in early October. During the longer periods of low-level westerly winds in September, the synoptic-scale variations in meridional wind are much less evident in these soundings, and during these longer periods of westerlies there is also some tendency toward easterly anomalies in the upper troposphere above the westerlies, though not precisely in phase; in the early September event, the upper-level easterlies lead the lower-level westerlies in time, whereas they lag in the late September event. The early October intraseasonal event, associated with upper tropospheric westerlies and lower tropospheric easterlies as identified in Fig. 7, is also clearly manifested in the zonal wind field in Fig. 10. The relative humidity anomalies are mostly positive through a deep midtropospheric layer during the early September westerly period and again around 1 October, although not during the period of westerly winds starting just after 22 September. The dry anomalies after 5 October appear consistent with onset of the MJO-like suppressed event defined in Fig. 7.

We focus now on the period of strong westerly winds in early September. Figure 11 shows visible satellite images and maps of zonal wind, geopotential, and OLR from 0000 UTC 1 September and 3 September, when Jebi's center was at 20°N and just north of 25°N, respectively. At its closest, Jebi's center was around 800 km away from the *Thompson*. A strong "monsoon tail" or belt of low-level westerlies to the south and southwest of the storm center was present during this time. A belt of low OLR was coincident with the westerlies during this whole period from 1–3 September, decaying over the next several days by retreating to the west. The visible images show the tops of the convective clouds associated with the low OLR; the impression of plumes trailing westward from the brightest convective cores is broadly consistent with the vertical shear that is apparent at this time upon inspection of Figs. 4, 5, and 10.

Extensions of monsoon westerly winds into the tropical western North Pacific, similar to those described above, have been previously observed in association with tropical cyclones. Xie et al. (1963), in what was apparently the first study to document a tropical intraseasonal oscillation, noted that enhanced typhoon development occurred when monsoon westerlies reached further eastward than average (see also Li et al. 2018). Reid et al. (2012) documented one such event in association with TC Lekima in fall of 2007 (see their Fig. 13). In that case, the belt of westerlies was connected to a region of strong westerly atmospheric flow and enhanced precipitation in the Bay of Bengal. In the present case, the westerly winds in the PISTON region were also connected to those over the Indian Ocean (Fig. 4). Cayanan et al. (2011) showed that the passage of tropical cyclones to the northeast of the Philippines are associated with a strengthening of the monsoon flow over the Philippines that can cause heavy rainfall over Luzon.

In some respects, these periods of strong westerly winds are similar to the westerly wind bursts familiar from the ENSO literature (e.g., Vecchi and Harrison 1997; Harrison and Vecchi 1997), but since they are centered well off the equator, we do not expect them to have much influence on the equatorial oceanic thermocline, and thus not on ENSO either.

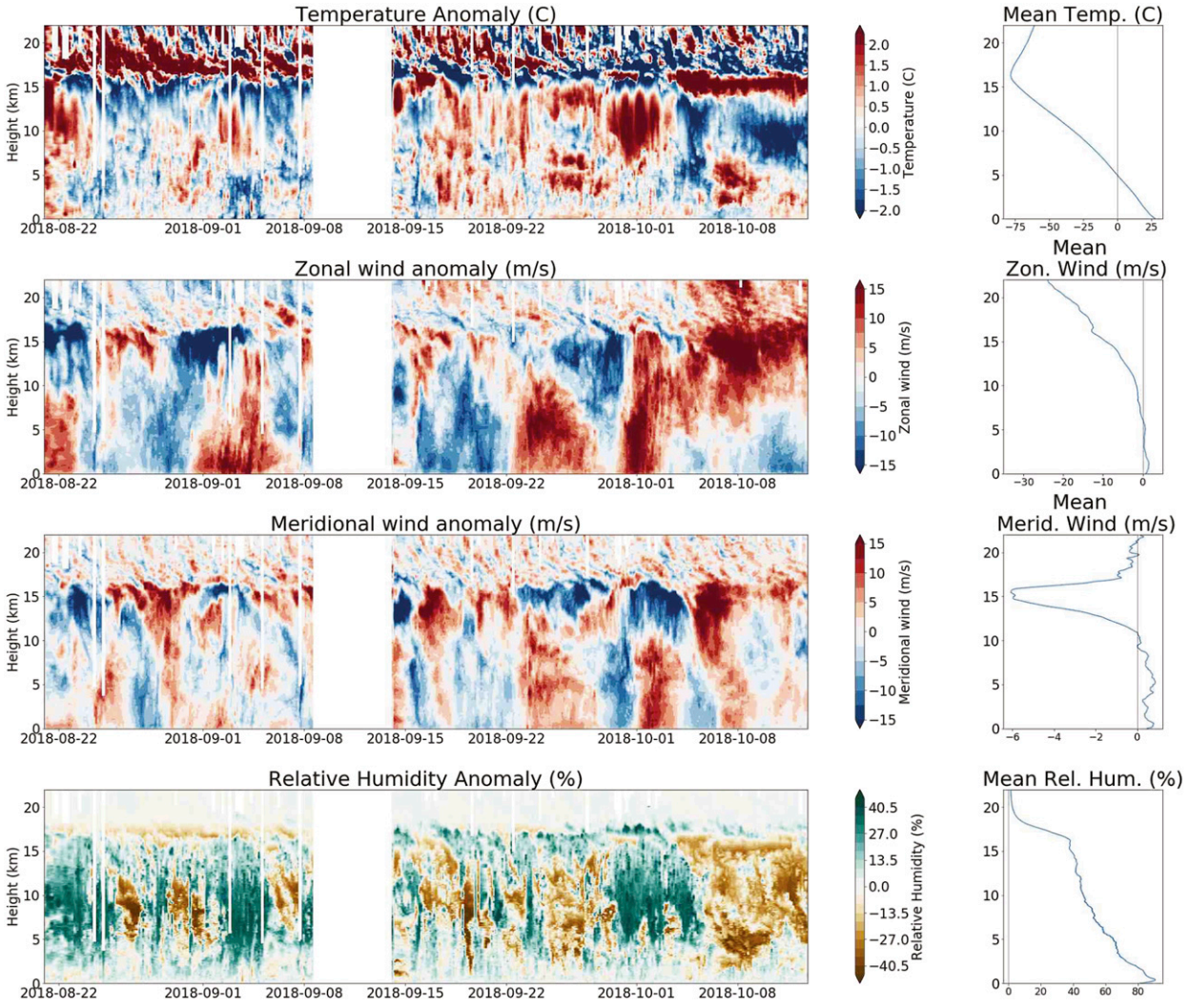

FIG. 10. (left) Anomalies of temperature (°C), zonal wind speed (m s^{-1}), meridional wind speed (m s^{-1}), and relative humidity (%), from the PISTON soundings. (right) Anomalies are computed as deviations from the time mean of the same data shown in the corresponding panels. All soundings are linearly interpolated onto the same vertical grid before plotting, formed by taking 3000 points linearly spaced from 0 to 22 000 m.

Nonetheless they are of interest since they occur at the locus of the Asian monsoon, tropical cyclones, and synoptic and intraseasonal variability. The outstanding question is the nature of the causal relationships between these phenomena. Sobel and Maloney (2000), for example, argued that periods when the monsoon westerlies extend farther or more strongly into the Pacific cause tropical cyclogenesis in that they stimulate the development of precursors by converging wave activity, but it has also been argued that a TC can induce the westerlies (e.g., Harrison and Giese 1991; Kindle and Phoebus 1995). The latter appears to perhaps be the case with Typhoon Trami, whose westerly wind anomalies were the largest during PISTON (Fig. 4). Those westerly wind anomalies were preceded in time by easterly anomalies, and were spatially disconnected from the monsoon westerlies to the west. We cannot determine the causality in general, however, nor the reason for the timing or quasi-periodicity of these events during PISTON. We can say, regarding the westerlies associated with Typhoon Jebi and shown in Fig. 11 in particular, that while it is plausible to associate this belt of westerlies with the storm, it is also apparent that this association cannot explain the entire evolution of this complex of atmospheric features, because the belt of westerlies persisted after the storm center had moved quite far north of it.

In situ observations from the *Thompson* during the cruise show how the zonal wind variations described above modulated the surface fluxes and the susceptibility of the atmosphere to deep convection. Figure 12 presents time series of wind speed and daily mean zonal wind; SST and surface air temperature; surface radiative, latent, and sensible heat fluxes; and precipitation (both 10-min and daily average precipitation; note the different units on the *y* axis). During the periods of strong low-level westerly winds in early September (e.g., Fig. 11) and early October, wind speed was enhanced in the extension of the monsoon westerlies (Fig. 12a) over

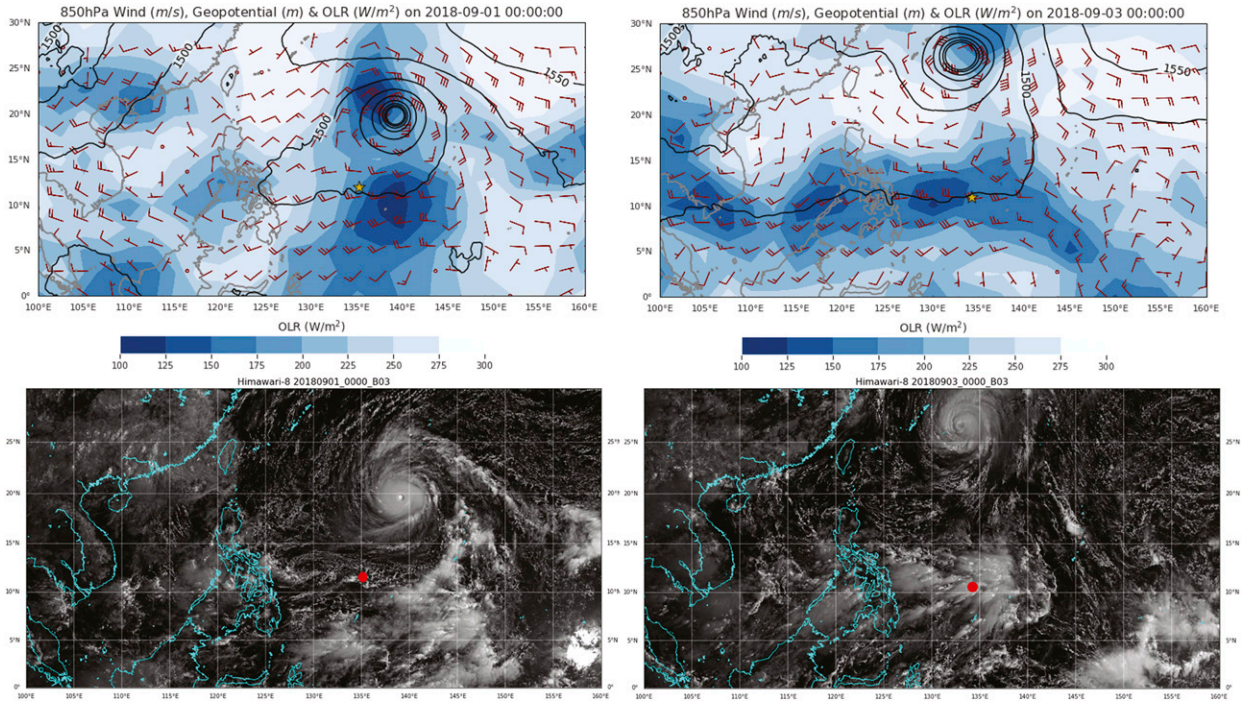

FIG. 11. (top left) Snapshot of 850-hPa wind (m s^{-1}; barbs—half barb is 2.5 m s^{-1}, full barb is 5 m s^{-1}), geopotential (m; contours), and OLR (W m^{-2}; shading) and (bottom left) visible (0.64 μm) satellite image from the advanced Himawari imager at 0000 UTC 1 Sep. (right) As in the left panels, but for 0000 UTC 3 Sep. The strong vortex in all panels is Typhoon Jebi. The yellow stars and red dots indicate the approximate location of the R/V *Thompson* on the date of interest.

the region occupied by the *Thompson*, driving more intense surface turbulent flux (Fig. 12c). The strong westerlies in September were associated with Typhoon Jebi, as in Fig. 11 and described above, and with Typhoon Kong-Rey in early October. (The gap in observations in mid-September between the two cruises occurred during the time when Typhoon Mangkhut was influencing the region and *Thompson* was in port, so no direct shipboard data are available in that case.) The surface fluxes and turbulent entrainment under enhanced wind cooled the ocean SST, and the convective clouds reduced the incident solar radiation (e.g., on 2–6 September and 30 September–2 October; Fig. 12c). Stronger winds and cloud shading at this time gradually reduced SST (Fig. 12b).

SST and air temperature both decreased following stronger winds and fluxes during early September and early October, but the feedback of the ocean back onto the atmosphere is not as easy to detect. Fluxes were not obviously reduced by the reduction in SST. This is consistent with prior studies showing that the turbulent heat fluxes are predominantly controlled by winds in this region on subseasonal time scales (e.g., Gao et al. 2019).

Wind dominates variations in the latent heat flux. The correlation coefficient of the latent heat flux $H_l = \rho L C_H U(q_s - q_a) = \rho L u_* q_*$ to the friction velocity u_* is $r(H_l, u_*) = 0.88$, explaining 77% of the variance. [Its correlation to wind speed is $r(H_l, U) = 0.86$.] The surface thermodynamic factors explain very little of the latent heat flux: latent heat flux is weakly anticorrelated to q_*, the moisture fluctuation scale (turbulent moisture flux divided by u_*), at $r(H_l, q_*) = -0.16$, and to sea–air specific humidity difference at $r(H_l, q_s - q_a) = 0.24$. The difference in the correlation between the two different thermodynamic factors reflects their different correlations to the wind speed. We expect the dynamically smaller sensible heat flux to behave similarly.

b. Oceanic conditions

The PISTON field campaign period corresponded to a period of ocean surface warming in the broader tropical Pacific associated with the onset of the 2018–19 El Niño event. The campaign was located in the warm pool region of the western tropical North Pacific where SST > 29°C is common during the typical September (Fig. 13). Although the PISTON study region was near its monthly average during September 2018, SST was anomalously warm (>0.5°) in the equatorial warm pool and most of the central to eastern tropical Pacific of the Northern Hemisphere (Fig. 13). These higher temperatures likely played a critical role in the genesis and evolution of the extraordinary number of category 5 storms observed in the northern tropical Pacific during the PISTON period (Fig. 9; see also Fig. S5). As noted above, 1997 was also a (major) El Niño onset year, and 1997 and 2018 are tied in the modern record for having the most category 5 super typhoons, a total of five, form during August–October. While the SST anomalies at this time of year were much warmer in the eastern equatorial Pacific during 1997 compared to 2018, there were also (weak) warm anomalies occurring north of the equator and west of the date line in 1997 (e.g., Wang and Weisberg 2000).

Anomalously strong monsoonal westerlies (Fig. 4) likely enhanced the surface turbulent heat flux, as well as

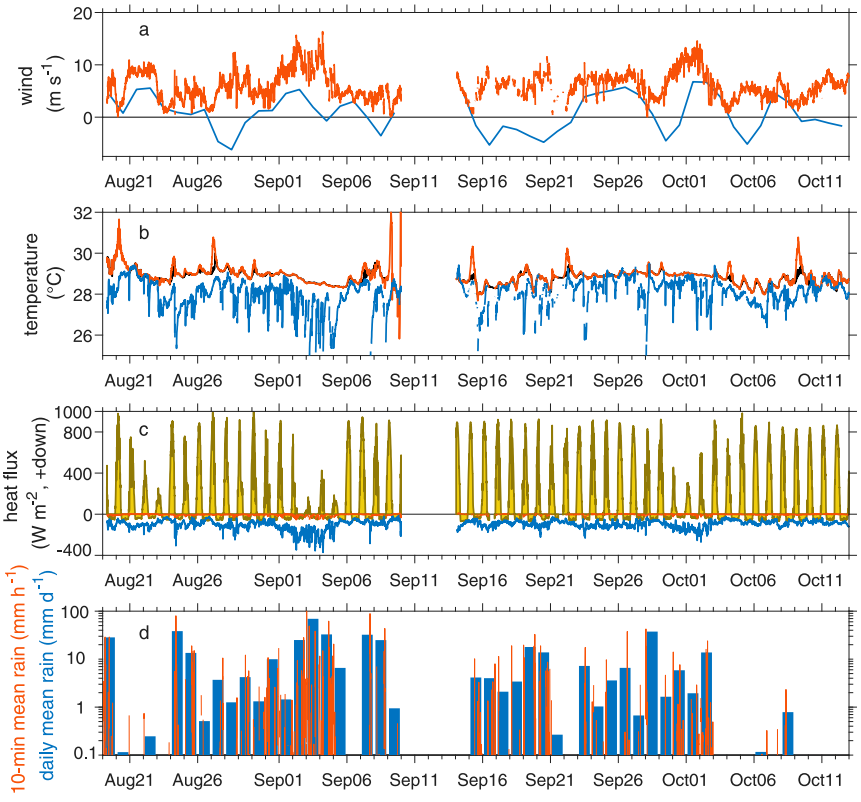

FIG. 12. (a) Surface wind speed (m s^{-1}; red) and daily mean zonal wind (m s^{-1}; blue); (b) SST (°C, red) and surface air temperature (°C; blue); (c) net radiative heating (W m^{-2}; filled yellow), surface evaporative cooling (W m^{-2}; blue), and sensible heat flux (W m^{-2}; red); and (d) 10-min (mm h^{-1}; red) and daily mean (mm day^{-1}; blue bars) rain observed at the R/V *Thompson* during the two legs of PISTON 2018. Note the different units for 10-min and daily precipitation values in (d). There is a 4-day hiatus in all observations 10–14 September during the port call.

entrainment of colder water from below the mixed layer, both contributing to the anomalously cool SST observed between 10° and 20°N (Fig. 14) before the *Thompson* surveyed along 135°E. Evidence of the passage of the tropical cyclones (Fig. 9) within the vicinity of the PISTON study region is also observed in the daily SST anomalies along 135°E (Fig. 14). In particular, the passage of Super Typhoon Mangkhut on 12 September 2018 through ~14°N, 135°W, which at that stage was a category 5 storm on the Saffir–Simpson wind scale (Fig. 9), was evident by anomalous cooling of more than 1°C that persisted for nearly a week. There was minimal recovery of the SST (Fig. 14) before the passage of Typhoon Trami, which passed through ~16.5°N, 135°E as a category 1 storm on 23 September 2018, and also Typhoon Kong-Rey, which passed through ~16°N, 135°E as a category 3–4 storm on 1 October 2018 (Fig. 9).

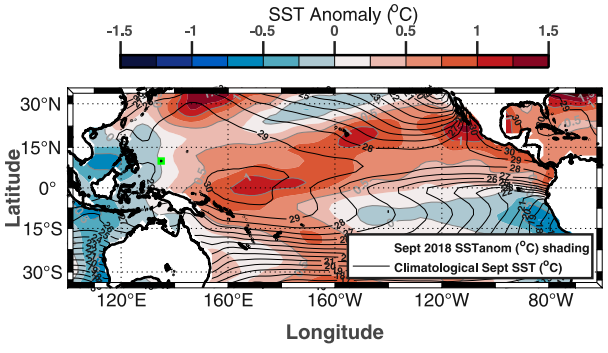

FIG. 13. Mean September climatology (contours) and anomalous September 2018 (shading) SST (°C) during the PISTON field campaign. Green square denotes the R/V *Thompson* intensive operations area, excluding transit.

The uCTD surveys along 135°E during the PISTON cruises offer the opportunity to explore the differences in oceanic conditions before and after the passage of Super Typhoon Mangkhut. The individual profiles were closely spaced and collected over only a day-long time interval along this fixed transect and so offer a more synoptic, Eulerian view of the response to this storm's passage in addition to the coarser temporal and Lagrangian view of the same storm offered by profiling float data (Johnston et al. 2020).

Although the four meridional uCTD transects along 135°E prior to the passage of Super Typhoon Mangkhut showed some

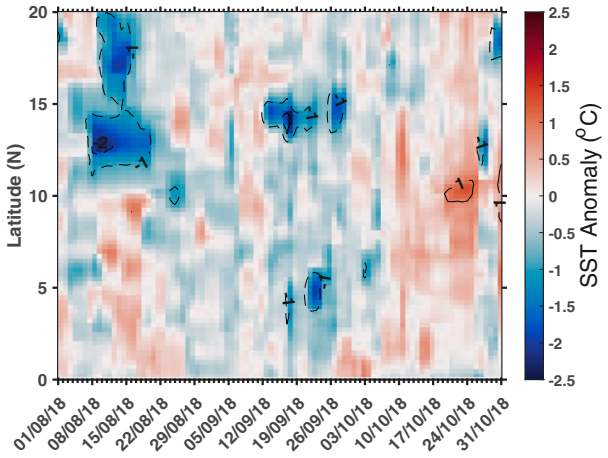

FIG. 14. Daily anomalous SST (°C) along 135°E during the PISTON field campaign.

variability, the survey along 135°E on 8 September 2018 serves to illustrate the ''typical'' subsurface temperature and salinity conditions in the PISTON study region (Figs. 15a,c,e). This transect, prior to Mangkhut, was characterized by a very fresh (Fig. 15a) and warm (Fig. 15c) surface layer in the upper ~50 m, particularly in the southern part of the transect. This is North Pacific Tropical Surface Water (NPTSW) that is thought to be sourced from either local rainfall or meridional advection (Delcroix and Hénin 1991). NPTSW overlies a tongue of relatively salty North Pacific Tropical Water (NPTW; Fig. 15a) found between the 20° and 25°C isotherms. The NPTW was thicker and saltier in the transect of 8 September 2018 (Fig. 15a) compared to the two transects undertaken earlier on 23 August and 29 August 2018 (not shown). The NPTW salinity maximum thermocline waters originate in the high evaporation regime at the center of the North Pacific subtropical gyre where the salty surface water is subducted and then advected around the subtropical gyre. The low salinity North Pacific Intermediate Water (NPIW) occupied the transect below the NPTW and is characterized by a tongue of salinity minima just below the 15°C isotherm that thins from north to south (Fig. 15a). NPIW is formed in the North Pacific subarctic (Talley 1993; Yasuda 1997), sinking along isopycnals to flow equatorward and merge with the subtropical circulation primarily north of 8°N along the western boundary of the tropical Pacific (Bingham and Lukas 1994; Fine et al. 1994; Zang et al. 2020).

The isotherms from the 8 September 2018 transect along 135°E prior to Mangkhut slope downward from south to north (Fig. 15c) consistent with thermal wind support of the westward flow in the North Equatorial Current (NEC). The NEC was also evident in the direct zonal velocity measurements from the shipboard ADCP (Fig. 15e). The NEC is the southern limb of the wind-driven North Pacific subtropical gyre; it bifurcates at the Philippine coast, with part of the flow entering the Kuroshio and part entering the Mindanao Current. Weak eastward flow appeared at subthermocline depths below the 15°C isotherm (Fig. 15e) and may be a manifestation of the North Equatorial Undercurrent (NEUC) jets that, in the mean, extend across the Pacific (Cravatte et al. 2012; Qiu et al. 2015).

The upper ocean properties and velocity sections during PISTON prior to Mangkhut did show some variability from transect to transect. In glider transects along 134.3°E north of Palau repeated over a 4-yr period, Schönau and Rudnick (2015) found that typically the strongest geostrophic velocity of the NEC was found in the upper 200 m from 9° to 13°N with eastward flow not unusual between 13° and 16.5°N. However, the location and strength of the westward flowing NEC jets changed and were often embedded within a broad slower background westward current. Our repeat ADCP velocity transects showed a similar wide variety in the NEC flow and in the presence of the NEUCs. Some of this variability might be attributed to current meandering or the presence of mesoscale eddies (Wyrtki 1982).

The uCTD survey on 14–16 September 2018, immediately after the passage of the category 5 Super Typhoon Mangkhut on 12 September 2018 through 14°N, 135°W (Fig. 9), shows that the storm had a dramatic impact on the oceanic properties (Figs. 15b,d,f). The relatively fresh and warmest (>28.5°C) near-surface layer became restricted to the southern part of the transect after the passage of Super Typhoon Mangkhut (Figs. 15b,d and 17a,b). The 28.5°C isotherm shoaled at ~13.5°N while cooler and saltier water was found to the north. In fact, there was a dramatic dip in the 25°C thermocline and deeper isotherms north of ~13.7°N after the passage of the storm.

The region north of ~14°N along 135°W was not surveyed prior to the passage of Mangkhut although two profiling floats that passed through this region prior to the storm show a warm upper ocean, with temperatures above 28.5°C, in the upper 100 m (Johnston et al. 2020) although they reported no salinity data. A direct comparison of two uCTD casts taken at 13°N, 135°E confirms that changes occurred in the profiles before and after the passage of Mangkhut (Fig. 16). After the storm, the surface layer was cooler, saltier, and denser in the upper ocean and well mixed in all properties down to ~66 m. In fact, SST (Fig. 17a) and sea surface salinity (SSS) (Fig. 17b) were cooler and saltier, respectively, along the entire 135°E transect after the passage of the storm. Below the mixed layer, the thermocline between 100–220 m shoaled by ~20–30 m after the storm (Fig. 16). Although the salinity maximum was located at ~125-m depth both before and after the storm, waters from the fresh NPIW were entrained with the rising thermocline and so freshened the layer immediately below the salinity maximum (Fig. 16).

The westward flowing NEC was much stronger in the southern part of the transect after the typhoon passage than before (Figs. 15e,f). A strongly sheared current developed afterward between 13.5° and ~15°N characterized by an eastward jet at 13.5°–14°N of ~0.5 m s^{-1} and a much stronger westward jet (>1 m s^{-1}) found to the north between 14° and 15°N (Fig. 15f). The westward flowing limb extended deeper in the water column compared to the eastward flow, and appears responsible for the dramatic deepening of the 25°C isotherm and the salty NPTW layer in the northern part of the transect following the passage of the storm (Figs. 15b,d). After the storm a strong westward flow developed in the upper 100 m and

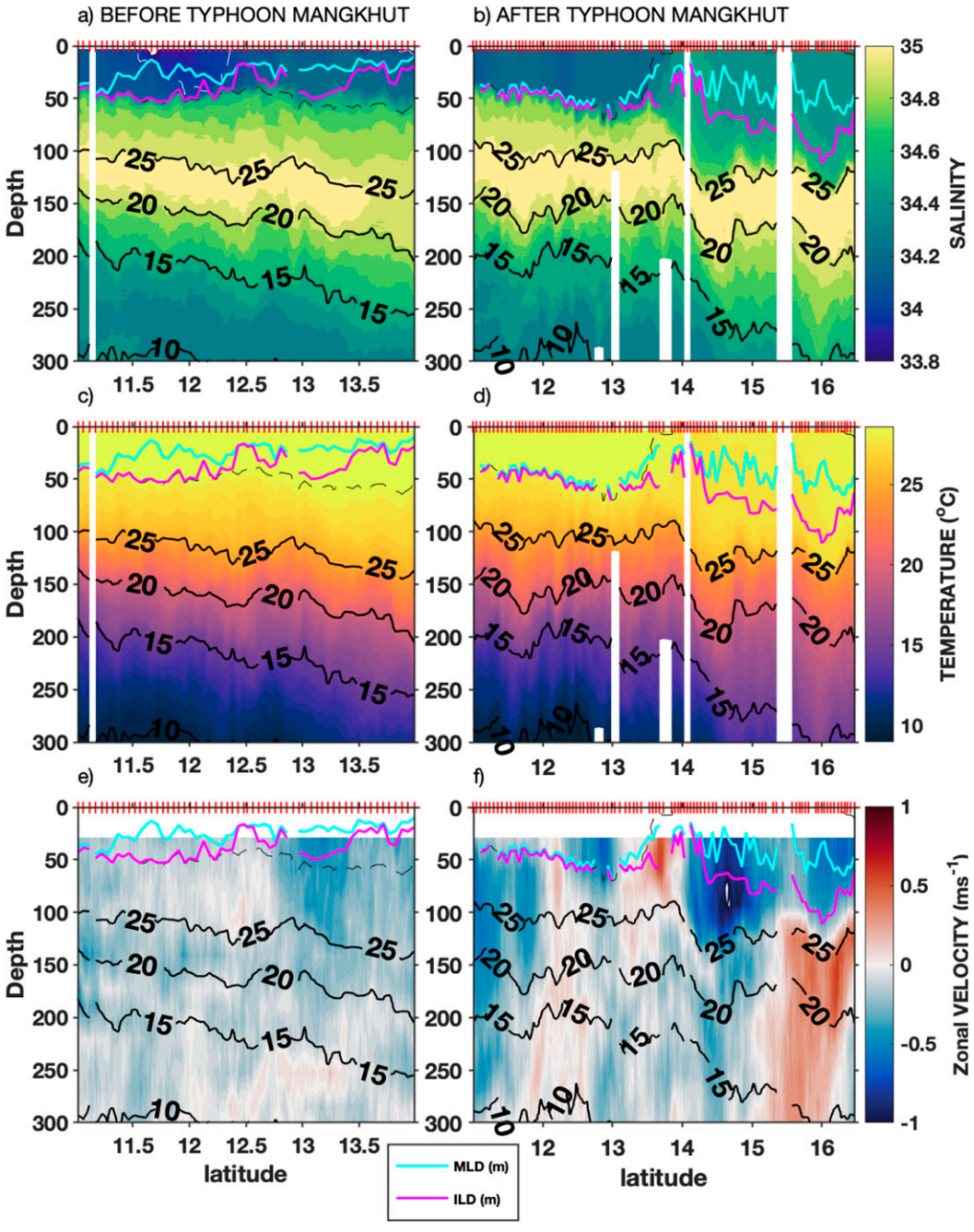

FIG. 15. uCTD (a),(b) salinity, (c),(d) temperature (°C), and (e),(f) ADCP velocity (m s^{-1}) from a shipboard survey along 135°E on (left) 8 Sep 2018 before the passage of Super Typhoon Mangkhut and (right) 14–16 Sep 2018 after the typhoon passed. Positive velocity [red in (e) and (f)] is eastward. Each panel has the 10°–25°C isotherms at contour intervals of 5°C (solid) and the 28.5°C (dashed) isotherm overlain. The red crosses at the top of the panels indicate the location of each uCTD cast. Note different latitudinal extent of pre and post-Mangkhut surveys. The mixed layer depth defined by density (cyan line) and the isothermal layer depth (magenta line) are indicated on each panel.

extended into the subthermocline layer to at least 400-m depth at the very northern end of the section with strong eastward flow found below (Fig. 15f). It is probable that this response in the velocity and shear is related to the generation and passage of near-inertial motions. Northern Hemisphere typhoons are known to form cold wakes along and to the right of the storm track through a combination of air–sea heat transfer, upwelling, and mixing. This is primarily because of the directional

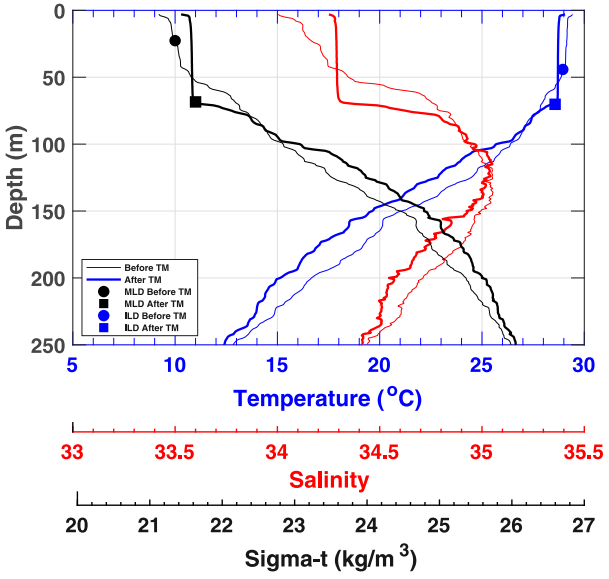

FIG. 16. Temperature (blue), salinity (red), and sigma-t (black) profiles at 13°N, 135°E before (light line) and after (heavy line) the passage of Super Typhoon Mangkhut. Symbols indicate the depth of the density defined mixed layer depth (black) and the temperature defined isothermal depth (blue) before (circle) and after (square) the storm.

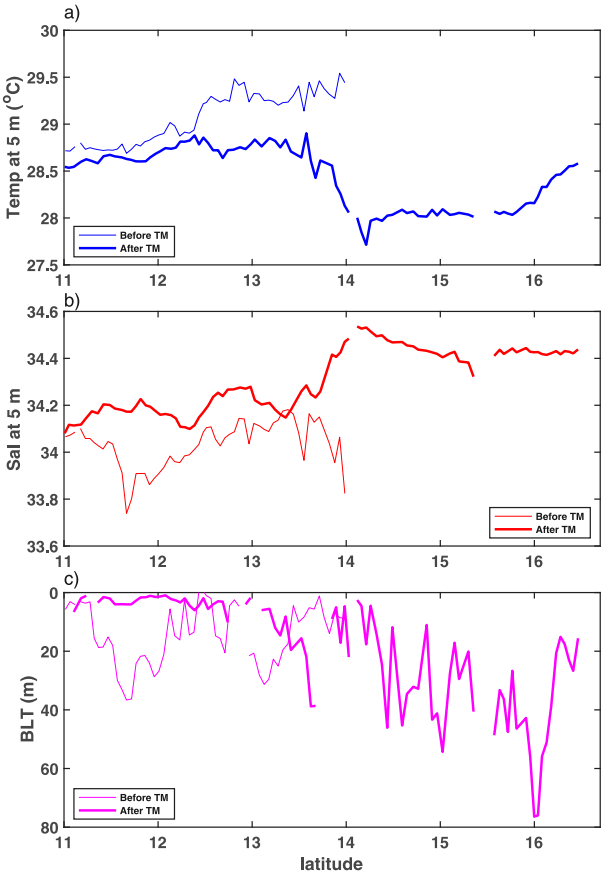

FIG. 17. (a) Temperature (°C) and (b) salinity at 5-m depth, and (c) barrier layer thickness (m) from the uCTD transects along 135°E before (light line) and after (heavy line) the passage of Super Typhoon Mangkhut.

alignment of the wind stress coupled with near-inertial motions on the right-hand side of a storm, whereas on the left side they can be opposed (Price 1981). The velocity response observed after Super Typhoon Mangkhut passed through at around 14°N, 135°E (Fig. 15f) show the expected bias of stronger motions in the cold wake on the right-hand side where speeds $> 1\,\mathrm{m\,s^{-1}}$ were observed. As a storm passes through a region, the surface near-inertial currents can propagate downward as internal gravity waves (Price 1983). The strong eastward current evident in the subthermocline layer between 15.5° and 16.5°N may be a delayed response after the storm passage.

Prior to the passage of Typhoon Mangkhut, the density-defined mixed layer depth (MLD) was much shallower than the isothermal layer depth (ILD), indicating the presence of an intervening barrier layer that is well-mixed in temperature but not in salinity (Figs. 15 and 16). Barrier layers can trap fluxes of heat, freshwater, and momentum in a thinner ocean surface layer, which enhances their impacts on SST and potentially also the subsequent air–sea interaction. Barrier layers reduce entrainment cooling through the base of the mixed layer as the water below the MLD in the barrier layer and above the ILD is the same temperature. In this region barrier layers are often formed by heavy precipitation (Lukas and Lindstrom 1991; Sprintall and Tomczak 1992). While barrier layers are observed throughout the year in the PISTON region there are seasonal fluctuations in thickness and horizontal extent (Katsura and Sprintall 2020). Prior to the typhoon, ILDs varied between 30 and 50 m deep, MLDs were ~20–30 m, and subsequently the barrier layer thickness was 10–20 m (Fig. 17c).

MLDs and ILDs between 11° and 13.5°N along 135°E were nearly twice as deep after the passage of Mangkhut than before (Figs. 15 and 16) and the barrier layer was eroded by the storm (Fig. 17c). After the passage of the storm, the MLD and ILD dramatically shoal around 13.7°N to ~20-m depth, coinciding roughly with the northern edge of the warm freshwater pool (Figs. 15b,d) and the flow changed from eastward to westward (Fig. 15f). North of 13.7°N, there was a steady deepening of the ILD and to some extent also in the MLD (Fig. 15), and thick barrier layers from 30 to 80 m are found in this part of the transect after the passage of the storm (Fig. 17c). This region to the north also lies to the right of the typhoon track where, as noted above, enhanced cooling due to turbulent entrainment can occur (Price 1981; D'Asaro 2003; D'Asaro et al. 2007). It is likely that this region experienced stronger mixed layer cooling, deepening of the ILD, and enhanced BL formation after the storm passage (Steffen and Bourassa 2018).

4. Conclusions

The PISTON field campaign occurred during the latter part of the west Pacific monsoon season in 2018, continuing through the end of the monsoon in October. The observations were taken in a region that does not have many in situ concurrent air–sea observations routinely, so PISTON offers a valuable dataset and provides rare insight into the atmospheric circulation, air–sea

interaction, and ocean physics in the region. In this study, we provide an overview of the large-scale conditions in the atmosphere and ocean during the field campaign. Our intent is to provide large-scale context for more detailed and local studies using the field observations, and also to characterize the state and behavior of the atmospheric and ocean in detail during this time. We view this study as an exercise in synoptic meteorology and physical oceanography of the deep tropics, extending to the subseasonal time scale.

The dominant modes of intraseasonal variability, the MJO and BSISO, were largely inactive during PISTON. One episode of an eastward-propagating MJO signal is identified by standard diagnostics in October, but it exhibited only the suppressed phase, associated with clear skies and low-level easterly winds, and no active phase immediately before or after it. Instead, the atmosphere in the region around the *Thompson* was characterized by alternating periods of low-level easterly and westerly wind anomalies on a 10–20-day time scale, particularly in the first half of the experiment. During easterly periods, weak synoptic-scale disturbances, characterized by fluctuations of the low-level meridional wind and OLR and otherwise exhibiting properties of easterly waves or tropical depression-type disturbances, moved past the ship with periods of a few days between the axes of the low-level troughs and ridges. The westerly wind periods were associated with eastward extensions of the monsoon westerlies occurring on the southern flanks of strong tropical cyclones.

The most dramatic westerly wind event that occurred during the PISTON cruises was in early September, associated with Typhoon Jebi. This episode resembled a westerly wind burst that might be associated with the MJO or ENSO, except for being centered around 10°N rather than the equator. The behavior observed here is also seen in other studies that have documented wind bursts in boreal summer at around 10°N (e.g., Vecchi and Harrison 1997; Harrison and Vecchi 1997; Cayanan et al. 2011; Reid et al. 2012). The strong westerly winds lasted for days after Typhoon Jebi had moved well to the north and was no longer directly connected to them. The strong surface winds, combined with strong cloud shading of the surface associated with frequent deep convection in the atmosphere, led to a net heat flux out of the ocean on the order of 200 $W m^{-2}$ lasting for a day or two. This net flux is comparable in magnitude to those observed in prior field campaigns during equatorial westerly wind bursts (Anderson et al. 1996; Moum et al. 2014; de Szoeke et al. 2015).

The PISTON period was one of extraordinarily strong tropical cyclone activity, particularly if measured by the record-tying number of category 5 super typhoons in the last 30 years. The large-scale westerly winds to the south and west of cyclones are representative of synoptic configuration of the monsoon wind patterns associated with the genesis of most tropical cyclones (Ritchie and Holland 1999). The storms' OLR signals project on the wavenumber–frequency bands associated with both the equatorial Rossby and combined mixed Rossby–gravity and tropical depression–type wave disturbances, but the causal interpretation of this is not yet clear. That is, the cyclones could be forming within favorable environments of large-scale waves, or the apparent large-scale waves could simply be artifacts of spectral decomposition of cyclones that formed for other reasons. More broadly, an overarching question for future research is whether there may be any causal relationship between the high tropical cyclone activity, the low-level westerly wind anomalies during the first half of PISTON, the absence of the BSISO, and/or any of the other aspects of the synoptic to subseasonal variability, and if so, what that relationship might be. Do any of those conditions cause any of the others, or can they be viewed as independent?

If there is a climate-scale explanation for the high level of tropical cyclone activity during PISTON in particular, it seems most likely to be in the strong positive SST anomalies north of the equator and east of the date line, upstream of the PISTON region as defined by the lower atmospheric winds that steer tropical disturbances and tropical cyclones. These positive SST anomalies could have been favorable to the creation and maintenance of TCs observed during PISTON in that they can be expected to have warmed and moistened the low levels of the atmosphere upstream of the PISTON region by enhancing surface fluxes there. The anomalously warm SST north of the equator and east of the date line occurred during the initial months of the 2018–19 El Niño event. Studies suggest that increased western North Pacific tropical cyclone activity can precede the onset of El Niño (Lian et al. 2019) and even influence the intensity of the El Niño (Sobel and Camargo 2005; Wang et al. 2019). The only other year in the last 30 years that matched the PISTON period in having five typhoons reach category 5 intensity during August–October was 1997, also the beginning of an El Niño event.

The tropical cyclones themselves induced strong local responses in the upper ocean, such as cooling, freshening, and deepening of the mixed layer. Persistent SST cooling after the passage of typhoons is related to the direct wind-driven entrainment of the cooler water from below. This ocean response is also dependent on the background ocean stratification, which can in turn feed back to affect subsequent air–sea interaction (Price 1981; D'Asaro 2003; D'Asaro et al. 2007; Vincent et al. 2012; Emanuel 2003; Domingues et al. 2019). In particular, Johnston et al. (2020) observed rapid upper ocean cooling from a profiling float array deployed over the PISTON period that suggested a decrease in the available potential energy to mix the water column after the passage of each successive storm. The impact on subsequent storms was amplified by the advection of the weakly stratified tropical cyclone wakes in the westward flowing NEC, the same direction as the passage of the typhoons (Johnston et al. 2020). However, while the development or intensification of any given tropical cyclone may have been inhibited when crossing the wake of a previous one—for example, when Typhoon Kong-Rey crossed the cold wake of Typhoon Trami around 130°E, 20°N—any such inhibition was not enough to prevent the formation of a record-tying number of category 5 storms. More broadly, the ocean surface in this region is nearly always warm enough, and the ocean mixed layer deep enough, that strong surface fluxes and deep atmospheric convection are possible, given adequate atmospheric triggers (e.g., strong surface winds to drive surface fluxes or synoptic- or mesoscale atmospheric disturbances to trigger deep convection). Consistent with these facts, previous studies have suggested that intraseasonal air–sea interactions in the PISTON region are weaker than in other basins such as the South China Sea and Indian Ocean (Duvel and Vialard 2007; Chou and Hseuh 2010).

The large-scale background currents alone are thought to have minimal impact on the ocean response to typhoons (e.g., Kunze 1985; Hormann et al. 2014; Baranowski et al. 2014). Rather, it is the generation and propagation of near-inertial oscillations driven in response to typhoon forcing that likely most impacts the velocity structure (Price 1981). Such direct velocity measurements of near-inertial motions driven by typhoons are relatively uncommon and are still poorly understood and modeled. The PISTON observations offer a rare glimpse of these features that might help to improve the prediction of the timing and strength of typhoons and their subsequent impact given the thermal response of the ocean.

Strong horizontal and vertical salinity gradients were observed during PISTON as a result of numerous processes including the presence and passage of storms, currents, fronts, and eddies. The increased stratification and stability associated with salinity-stratified barrier layers is thought to reduce the SST and mixed layer cooling during the passage of tropical storms (Balaguru et al. 2012, 2020). However, it remains a point of contention whether or not this subsequently affects air–sea interaction and tropical storm intensification (e.g., Grodsky et al. 2012; Hernandez et al. 2016). The feedback from the barrier layer to storm intensification appears dependent on the intensity and propagation speed of the storm itself as well as the prior ocean stratification including the depth of the mixed layer and available heat content (e.g., Steffen and Bourassa 2018; Balaguru et al. 2012, 2014, 2020; Bender and Ginis 2000; Yan et al. 2017; Baranowski et al. 2014; Chen et al. 2017).

The PISTON field observations provide unique opportunities to examine the ocean response to tropical cyclones and other phenomena. In this descriptive study, we have presented and interpreted the observations in light of phenomena known from prior literature on the weather and climate of the western North Pacific basin. This provides useful context for more in-depth studies using both the field observations and numerical models. Coordinated modeling efforts to target the phenomena observed during PISTON, under these representative large-scale conditions, will help answer key questions on the nature and degree of atmosphere–ocean coupling, and of the interaction between the tropical cyclones and larger scales.

Acknowledgments. AHS, SW, and ZKM's participation in PISTON is supported by the Office of Naval Research Award N00014-16-1-3073. JS's participation in PISTON is supported through the NOAA CVP Award NA17OAR431025. EDM's participation in PISTON and this study is supported by the Office of Naval Research Award number 00014-16-1-3087 and through NOAA CVP Award NA18OAR4310299. SD's participation is supported by the Office of Naval Research Award number N00014-16-1-3094. BCT's participation in PISTON is supported by the Office of Naval Research Award N000141613033. SAR's participation in PISTON is supported by the Office of Naval Research Award N00014-16-1-3092.

Data availability statement. The ERA5 dataset is publicly available though the Copernicus data portal, https://doi.org/10.24381/cds.bd0915c6.

The NOAA observed OLR dataset is available at https://psl.noaa.gov/data/gridded/data.interp_OLR.html.

The TRMM dataset (TRMM 2011) was retrieved via NASA's Earth Data website at https://earthdata.nasa.gov, distributed by the Goddard Earth Sciences Data and Information Services Center (GES DISC) at https://disc.gsfc.nasa.gov.

The best track dataset for western North Pacific tropical cyclones from JTWC can be found at https://www.metoc.navy.mil/jtwc/jtwc.html?western-pacific.

CODAS software and documentation to process shipboard ADCP data can be found at https://currents.soest.hawaii.edu/docs/adcp_doc/index.html.

Meteorology and surface flux data collected aboard the *Thompson* is available at the NOAA Physical Sciences Laboratory (PSL) ftp site: ftp://ftp1.esrl.noaa.gov/psd3/cruises/PISTON_MISOBOB_2018/TGT/.

All shipboard uCTD, ADCP and shipboard-deployed sonde data are available at https://doi.org/10.5067/SUBORBITAL/PISTON2018-ONR-NOAA/RVTHOMPSON/DATA001.

REFERENCES

Anderson, S. P., R. A. Weller, and R. B. Lukas, 1996: Surface buoyancy forcing and the mixed layer of the western Pacific warm pool: Observation and one-dimensional model results. *J. Climate*, **9**, 3056–3085, https://doi.org/10.1175/1520-0442(1996)009<3056:SBFATM>2.0.CO;2.

Balaguru, K., and Coauthors, 2012: Ocean barrier layer's effect on tropical cyclone intensification. *Proc. Nat. Acad. Sci.*, **109**, 14 343–14 347, https://doi.org/10.1073_FPNAS.1201364109.

——, S. Taraphdar, L. R. Leung, G. R. Foltz, and J. A. Knaff, 2014: Cyclone–cyclone interactions through the ocean pathway. *Geophys. Res. Lett.*, **41**, 6855–6862, https://doi.org/10.1002/2014GL061489.

——, G. R. Foltz, L. R. Leung, J. Kaplan, and W. Xu, 2020: Pronounced impact of salinity on rapidly intensifying tropical cyclones. *Bull. Amer. Meteor. Soc.*, **101**, E1497–E1511, https://doi.org/10.1175/BAMS-D-19-0303.1.

Banzon, V., T. M. Smith, T. M. Chin, C. Liu, and W. Hankins, 2016: A long-term record of blended satellite and in situ sea-surface temperature for climate monitoring, modeling and environmental studies. *Earth Syst. Sci. Data*, **8**, 165–176, https://doi.org/10.5194/essd-8-165-2016.

Baranowski, D. B., P. J. Flatau, S. Chen, and P. G. Black, 2014: Upper ocean response to the passage of two sequential typhoons. *Ocean Sci.*, **10**, 559–570, https://doi.org/10.5194/os-10-559-2014.

Bender, M. A., and I. Ginis, 2000: Real-case simulations of hurricane–ocean interaction using a high-resolution coupled model: Effects on hurricane intensity. *Mon. Wea. Rev.*, **128**, 917–946, https://doi.org/10.1175/1520-0493(2000)128<0917:RCSOHO>2.0.CO;2.

Bingham, F. M., and R. Lukas, 1994: The southward intrusion of North Pacific Intermediate Water along the Mindanao coast. *J. Phys. Oceanogr.*, **24**, 141–154, https://doi.org/10.1175/1520-0485(1994)024<0141:TSIONP>2.0.CO;2.

Cayanan, E. O., T.-C. Chen, J. C. Argete, M.-C. Yen, and P. D. Nilo, 2011: The effect of tropical cyclones on southwest monsoon rainfall in the Philippines. *J. Meteor. Soc. Japan*, **89A**, 123–139, https://doi.org/10.2151/jmsj.2011-A08.

Chen, S., R. L. Elsberry, and P. A. Harr, 2017: Modeling interaction of a tropical cyclone with its cold wake. *J. Atmos. Sci.*, **74**, 3981–4001, https://doi.org/10.1175/JAS-D-16-0246.1.

Chou, C., and Y.-C. Hsueh, 2010: Mechanisms of northward-propagating intraseasonal oscillation—A comparison between the Indian Ocean and the western North Pacific. *J. Climate*, **23**, 6624–6640, https://doi.org/10.1175/2010JCLI3596.1.

Ciesielski, P. E., and Coauthors, 2014: Quality-controlled upper-air sounding dataset for DYNAMO/CINDY/AMIE: Development and corrections. *J. Atmos. Oceanic Technol.*, **31**, 741–764, https://doi.org/10.1175/JTECH-D-13-00165.1.

Cravatte, S., W. S. Kessler, and F. Marin, 2012: Intermediate zonal jets in the tropical Pacific Ocean observed by Argo floats. *J. Phys. Oceanogr.*, **42**, 1475–1485, https://doi.org/10.1175/JPO-D-11-0206.1.

D'Asaro, E. A., 2003: The ocean boundary layer below Hurricane Dennis. *J. Phys. Oceanogr.*, **33**, 561–579, https://doi.org/10.1175/1520-0485(2003)033<0561:TOBLBH>2.0.CO;2.

——, T. B. Sanford, P. P. Niiler, and E. J. Terrill, 2007: Cold wake of Hurricane Frances. *Geophys. Res. Lett.*, **34**, L15609, https://doi.org/10.1029/2007GL030160.

Delcroix, T., and C. Hénin, 1991: Seasonal and interannual variations of sea surface salinity in the tropical Pacific Ocean. *J. Geophys. Res.*, **96**, 22 135–22 150, https://doi.org/10.1029/91JC02124.

de Szoeke, S. P., J. B. Edson, J. R. Marion, C. W. Fairall, and L. Bariteau, 2015: The MJO and air–sea interaction in TOGA COARE and DYNAMO. *J. Climate*, **28**, 597–622, https://doi.org/10.1175/JCLI-D-14-00477.1.

Dickinson, M., and J. Molinari, 2002: Mixed Rossby–gravity waves and western Pacific tropical cyclogenesis. Part I: Synoptic evolution. *J. Atmos. Sci.*, **59**, 2183–2196, https://doi.org/10.1175/1520-0469(2002)059<2183:MRGWAW>2.0.CO;2.

Domingues, R., and Coauthors, 2019: Ocean observations in support of studies and forecasts of tropical and extratropical cyclones. *Front. Mar. Sci.*, **6**, 446, https://doi.org/10.3389/fmars.2019.00446.

Duvel, J., and J. Vialard, 2007: Indo-Pacific sea surface temperature perturbations associated with intraseasonal oscillations of tropical convection. *J. Climate*, **20**, 3056–3082, https://doi.org/10.1175/JCLI4144.1.

Edson, J. B., and Coauthors, 2013: On the exchange of momentum over the open ocean. *J. Phys. Oceanogr.*, **43**, 1589–1610, https://doi.org/10.1175/JPO-D-12-0173.1.

Emanuel, K. A., 2003: Tropical cyclones. *Annu. Rev. Earth Planet. Sci.*, **31**, 75–104, https://doi.org/10.1146/annurev.earth.31.100901.141259.

Fairall, C. W., E. F. Bradley, J. S. Godfrey, G. A. Wick, J. B. Edson, and G. S. Young, 1996: Cool-skin and warm-layer effects on sea surface temperature. *J. Geophys. Res.*, **101**, 1295–1308, https://doi.org/10.1029/95JC03190.

——, S. Pezoa, L. Bariteau, D. E. Wolfe, and R. A. Weller, 2012: Evaluation of the accuracy of research vessels as in situ sources of surface flux observations from recent PSD cruises. *2010 Fall Meeting*, San Francisco, CA, Amer. Geophys. Union, Abstract OS51E-1923, https://ui.adsabs.harvard.edu/abs/2012AGUFMOS51E1923F/abstract.

Fine, R. A., R. Lukas, F. M. Bingham, M. J. Warner, and R. H. Gammon, 1994: The western equatorial Pacific: A water mass crossroads. *J. Geophys. Res.*, **99**, 25 063–25 080, https://doi.org/10.1029/94JC02277.

Gao, Y., N. P. Klingaman, C. A. DeMott, and P.-C. Hsu, 2019: Diagnosing ocean feedbacks to the BSISO: SST-modulated surface fluxes and the moist static energy budget. *J. Geophys. Res. Atmos.*, **124**, 146–170, https://doi.org/10.1029/2018JD029303.

Grodsky, S. A., and Coauthors, 2012: Haline hurricane wake in the Amazon/Orinoco plume: AQUARIUS/SACD and SMOS observations. *Geophys. Res. Lett.*, **39**, L20603, https://doi.org/10.1029/2012GL053335.

Harrison, D. E., and B. S. Giese, 1991: Episodes of surface westerly winds as observed from islands in the western tropical Pacific. *J. Geophys. Res.*, **96**, 3221–3237, https://doi.org/10.1029/90JC01775.

——, and G. A. Vecchi, 1997: Westerly wind events in the tropical Pacific, 1986–95. *J. Climate*, **10**, 3131–3156, https://doi.org/10.1175/1520-0442(1997)010<3131:WWEITT>2.0.CO;2.

Hernandez, O., J. Jouanno, and F. Durand, 2016: Do the Amazon and Orinoco freshwater plumes really matter for hurricane-induced ocean surface cooling? *J. Geophys. Res. Oceans*, **121**, 2119–2141, https://doi.org/10.1002/2015JC011021.

Hersbach, H., and Coauthors, 2020: The ERA5 global reanalysis. *Quart. J. Roy. Meteor. Soc.*, **146**, 1999–2049, https://doi.org/10.1002/qj.3803.

Hormann, V., L. R. Centurioni, L. Rainville, C. M. Lee, and L. J. Braasch, 2014: Response of upper ocean currents to Typhoon Fanapi. *Geophys. Res. Lett.*, **41**, 3995–4003, https://doi.org/10.1002/2014GL060317.

Johnston, S., D. L. Rudnick, N. Brizuela, and J. N. Moum, 2020: Advection by the North Equatorial Current of a cold wake due to multiple typhoons in the western Pacific: Measurements from a profiling float array. *J. Geophys. Res. Oceans*, **125**, e2019JC015534, https://doi.org/10.1029/2019JC015534.

Katsura, S., and J. Sprintall, 2020: Seasonality and formation of barrier layers and associated temperature inversions in the eastern tropical North Pacific. *J. Phys. Oceanogr.*, **50**, 791–808, https://doi.org/10.1175/JPO-D-19-0194.1.

Kikuchi, K., and B. Wang, 2010: Formation of tropical cyclones in the northern Indian Ocean associated with two types of tropical intraseasonal oscillation modes. *J. Meteor. Soc. Japan*, **88**, 475–496, https://doi.org/10.2151/jmsj.2010-313.

——, ——, and Y. Kajikawa, 2012: Bimodal representation of the tropical intraseasonal oscillation. *Climate Dyn.*, **38**, 1989–2000, https://doi.org/10.1007/s00382-011-1159-1.

Kiladis, G., J. Dias, K. H. Straub, M. C. Wheeler, S. N. Tulich, K. Kikuchi, K. M. Weickmann, and M. J. Ventrice, 2014: A comparison of OLR and circulation-based indices for tracking the MJO. *Mon. Wea. Rev.*, **142**, 1697–1715, https://doi.org/10.1175/MWR-D-13-00301.1.

Kindle, J. C., and P. A. Phoebus, 1995: The ocean response to operational westerly wind bursts during the 1991–1992 El Niño. *J. Geophys. Res.*, **100**, 4893–4920, https://doi.org/10.1029/94JC02392.

Kunze, E., 1985: Near-inertial wave propagation in geostrophic shear. *J. Phys. Oceanogr.*, **15**, 544–565, https://doi.org/10.1175/1520-0485(1985)015<0544:NIWPIG>2.0.CO;2.

Lau, K.-H., and N.-C. Lau, 1990: Observed structure and propagation characteristics of tropical summertime synoptic-scale disturbances. *Mon. Wea. Rev.*, **118**, 1888–1913, https://doi.org/10.1175/1520-0493(1990)118<1888:OSAPCO>2.0.CO;2.

——, and ——, 1992: The energetics and propagation dynamics of tropical summertime synoptic-scale disturbances. *Mon. Wea. Rev.*, **120**, 2523–2539, https://doi.org/10.1175/1520-0493(1992)120<2523:TEAPDO>2.0.CO;2.

Lee, J.-Y., B. Wang, M. C. Wheeler, X. Fu, D. E. Waliser, and I.-S. Kang, 2013: Real-time multivariate indices for the boreal summer intraseasonal oscillation over the Asian summer monsoon region. *Climate Dyn.*, **40**, 493–509, https://doi.org/10.1007/s00382-012-1544-4.

Li, T., L. Wang, M. Peng, B. Wang, C. Zhang, W. Lau, and H.-C. Kuo, 2018: A paper on the tropical intraseasonal oscillation published in 1963 in a Chinese journal. *Bull. Amer. Meteor. Soc.*, **99**, 1765–1779, https://doi.org/10.1175/BAMS-D-17-0216.1.

Lian, T., J. Ying, H.-L. Ren, C. Zhang, T. Liu, and X.-X. Tan, 2019: Effects of tropical cyclones on ENSO. *J. Climate*, **32**, 6423–6443, https://doi.org/10.1175/JCLI-D-18-0821.1.

Liebmann, B., and C. A. Smith, 1996: Description of a complete (interpolated) outgoing longwave radiation dataset. *Bull. Amer. Meteor. Soc.*, **77**, 1275–1277, https://doi.org/10.1175/1520-0477-77.6.1274.

Liu, Z., D. Ostrenga, W. Teng, and S. Kempler, 2012: Tropical Rainfall Measuring Mission (TRMM) precipitation data and services for research and applications. *Bull. Amer. Meteor. Soc.*, **93**, 1317–1325, https://doi.org/10.1175/BAMS-D-11-00152.1.

Lukas, R., and E. Lindstrom, 1991: The mixed layer of the western equatorial Pacific Ocean. *J. Geophys. Res.*, **96**, 3343–3357, https://doi.org/10.1029/90JC01951.

Moon, J.-Y., B. Wang, K.-J. Ha, and J.-Y. Lee, 2013: Teleconnections associated with Northern Hemisphere summer monsoon intraseasonal oscillation. *Climate Dyn.*, **40**, 2761–2774, https://doi.org/10.1007/s00382-012-1394-0.

Moum, J. N., and Coauthors, 2014: Air–sea interactions from westerly wind bursts during the November 2011 MJO in the Indian Ocean. *Bull. Amer. Meteor. Soc.*, **95**, 1185–1199, https://doi.org/10.1175/BAMS-D-12-00225.1.

Payne, R. E., 1972: Albedo of the sea surface. *J. Atmos. Sci.*, **29**, 959–970, https://doi.org/10.1175/1520-0469(1972)029<0959:AOTSS>2.0.CO;2.

Price, J. F., 1981: Upper ocean response to a hurricane. *J. Phys. Oceanogr.*, **11**, 153–175, https://doi.org/10.1175/1520-0485(1981)011<0153:UORTAH>2.0.CO;2.

——, 1983: Internal wave wake of a moving storm. Part I: Scales, energy budget and observations. *J. Phys. Oceanogr.*, **13**, 949–965, https://doi.org/10.1175/1520-0485(1983)013<0949:IWWOAM>2.0.CO;2.

Qiu, B., D. L. Rudnick, I. Cerovecki, B. Cornuelle, S. Chen, M. Schonau, J. McClean, and G. Gopalakrishnan, 2015: The Pacific North Equatorial Current: New insights from the Origins of the Kuroshio and Mindanao Currents (OKMC) project. *Oceanography*, **28**, 24–33, https://doi.org/10.5670/oceanog.2015.78.

Ramsay, H. A., 2017: The global climatology of tropical cyclones. *Oxford Research Encyclopedia of Natural Hazard Science*, Oxford University Press, https://doi.org/10.1093/acrefore/9780199389407.013.79.

Reed, R. J., and E. E. Recker, 1971: Structure and properties of synoptic-scale wave disturbances in the equatorial western Pacific. *J. Atmos. Sci.*, **28**, 1117–1133, https://doi.org/10.1175/1520-0469(1971)028<1117:SAPOSS>2.0.CO;2.

Reid, J. S., and Coauthors, 2012: Multi-scale meteorological conceptual analysis of observed active fire hotspot activity and smoke optical depth in the Maritime Continent. *Atmos. Chem. Phys.*, **12**, 2117–2147, https://doi.org/10.5194/acp-12-2117-2012.

Reynolds, R. W., T. M. Smith, C. Liu, D. B. Chelton, K. S. Casey, and M. G. Schlax, 2007: Daily high-resolution blended analyses for sea surface temperature. *J. Climate*, **20**, 5473–5496, https://doi.org/10.1175/2007JCLI1824.1.

Ritchie, E. A., and G. J. Holland, 1999: Large-scale patterns associated with tropical cyclogenesis in the western Pacific. *Mon. Wea. Rev.*, **127**, 2027–2043, https://doi.org/10.1175/1520-0493(1999)127<2027:LSPAWT>2.0.CO;2.

Schönau, M. C., and D. L. Rudnick, 2015: Glider observations of the North Equatorial Current in the western tropical Pacific. *J. Geophys. Res. Oceans*, **120**, 3586–3605, https://doi.org/10.1002/2014JC010595.

Schott, T., and Coauthors, 2019: The Saffir–Simpson Hurricane Wind Scale. 4 pp., http://www.nhc.noaa.gov/pdf/sshws.pdf.

Sobel, A. H., and C. S. Bretherton, 1999: Development of synoptic-scale disturbances over the summertime tropical northwest Pacific. *J. Atmos. Sci.*, **56**, 3106–3127, https://doi.org/10.1175/1520-0469(1999)056<3106:DOSSDO>2.0.CO;2.

——, and E. D. Maloney, 2000: Effect of ENSO and the MJO on western North Pacific tropical cyclones. *Geophys. Res. Lett.*, **27**, 1739–1742, https://doi.org/10.1029/1999GL011043.

——, and S. J. Camargo, 2005: Influence of western North Pacific tropical cyclones on their large-scale environment. *J. Atmos. Sci.*, **62**, 3396–3407, https://doi.org/10.1175/JAS3539.1.

Sprintall, J., and M. Tomczak, 1992: Evidence of the barrier layer in the surface layer of the tropics. *J. Geophys. Res.*, **97**, 7305–7316, https://doi.org/10.1029/92JC00407.

Steffen, J., and M. Bourassa, 2018: Barrier layer development local to tropical cyclones based on Argo float observations. *J. Phys. Ocean.*, **48**, 1951–1968, https://doi.org/10.1175/JPO-D-17-0262.1.

Takayabu, Y. N., and T. Nitta, 1993: 3–5 day period disturbances coupled with convection over the tropical Pacific Ocean. *J. Meteor. Soc. Japan*, **71**, 221–246, https://doi.org/10.2151/jmsj1965.71.2_221.

Talley, L. D., 1993: Distribution and formation of North Pacific Intermediate Water. *J. Phys. Oceanogr.*, **23**, 517–537, https://doi.org/10.1175/1520-0485(1993)023<0517:DAFONP>2.0.CO;2.

TRMM, 2011: Tropical Rainfall Measuring Mission (TRMM). TRMM (TMPA) rainfall estimate L3 3 hour 0.25 degree × 0.25 degree V7, Goddard Earth Sciences Data and Information Services Center (GES DISC), accessed 6 June 2019, https://doi.org/10.5067/TRMM/TMPA/3H/7.

Ullman, D. S., and D. Hebert, 2014: Processing of underway CTD data. *J. Atmos. Oceanic Technol.*, **31**, 984–998, https://doi.org/10.1175/JTECH-D-13-00200.1.

Vecchi, G. A., and D. E. Harrison, 1997: Westerly wind events in the tropical Pacific, 1986–1995: An atlas. Tech. Rep. NOAA/PMEL Tech. Memo. ERL PMEL-109, 222 pp.

Vincent, E. M., M. Lengaigne, J. Vialard, G. Madec, N. C. Jourdain, and S. Masson, 2012: Assessing the oceanic control on the amplitude of sea surface cooling induced by tropical cyclones. *J. Geophys. Res.*, **117**, C05023, https://doi.org/10.1029/2011JC007705.

Wang, B., and X. Xie, 1997: A model for the boreal summer intraseasonal oscillation. *J. Atmos. Sci.*, **54**, 72–86, https://doi.org/10.1175/1520-0469(1997)054<0072:AMFTBS>2.0.CO;2.

Wang, C., and R. H. Weisberg, 2000: The 1997–98 El Niño evolution relative to previous El Niño events. *J. Climate*, **13**, 488–501, https://doi.org/10.1175/1520-0442(2000)013<0488:TENOER>2.0.CO;2.

Wang, Q., and Coauthors, 2019: Tropical cyclones act to intensify El Niño. *Nat. Commun.*, **10**, 3793, https://doi.org/10.1038/s41467-019-11720-w.

Wang, S., D. Ma, A. H. Sobel, and M. K. Tippett, 2018: Propagation characteristics of BSISO indices. *Geophys. Res. Lett.*, **45**, 9934–9943, https://doi.org/10.1029/2018GL078321.

Wheeler, M. C., and H. H. Hendon, 2004: An all-season real-time multivariate MJO index: Development of an index for monitoring and prediction. *Mon. Wea. Rev.*, **132**, 1917–1932, https://doi.org/10.1175/1520-0493(2004)132,1917:AARMMI.2.0.CO;2.

——, G. N. Kiladis, and P. J. Webster, 2000: Large-scale dynamical fields associated with convectively coupled equatorial waves. *J. Atmos. Sci.*, **57**, 613–640, https://doi.org/10.1175/1520-0469(2000)057,0613:LSDFAW.2.0.CO;2.

Wyrtki, K., 1982: Eddies in the Pacific North Equatorial Current. *J. Phys. Oceanogr.*, **12**, 746–749, https://doi.org/10.1175/1520-0485(1982)012<0746:EITPNE>2.0.CO;2.

Xie, Y.-B., S.-J. Chen, I.-L. Zhang, and Y.-L. Hung, 1963: A preliminarily statistic and synoptic study about the basic currents over southeastern Asia and the initiation of typhoon (in Chinese). *Acta Meteor. Sin.*, **33**, 206–217.

Yan, Y., L. Li, and C. Wang, 2017: The effects of oceanic barrier layer on the upper ocean response to tropical cyclones. *J. Geophys. Res. Oceans*, **122**, 4829–4844, https://doi.org/10.1002/2017JC012694.

Yasuda, I., 1997: The origin of the North Pacific Intermediate Water. *J. Geophys. Res.*, **102**, 893–909, https://doi.org/10.1029/96JC02938.

Zang, N., F. Wang, and J. Sprintall, 2020: The intermediate water in the Philippine Sea. *J. Oceanol. Limnol.*, **38**, 1343–1353, https://doi.org/10.1007/s00343-020-0035-4.